4.0 WAVE TRANSFORMATION NUMERICAL MODELING

4.1 ANALYSIS APPROACH

A quantitative understanding of wave characteristics, storm surge, sediment transport, and other natural processes is key to implementing an effective borrow site management plan. Computer models provide predictive tools for evaluating various forces governing wave climate, sediment transport processes, and the performance of beach fill extraction from offshore borrow sites. Quantitative information produced from numerical models can be used to maximize the design life of beach replenishment projects and examine the effects of dredging at offshore borrow sites. As a result, management strategies can be developed to explain the physical processes that dominate a region and to furnish appropriate recommendations/solutions for each stretch of coast.

An assessment of potential impacts caused by dredging offshore borrow sites can be determined using wave modeling to estimate refraction, diffraction, shoaling, and wave breaking. Refraction and diffraction may have a significant effect on the impacts waves have on a shoreline. Wave refraction and diffraction generally result in an uneven distribution of wave energy along the coast that affects sediment transport in the region. Wave modeling results provide information on wave propagation across the continental shelf and to the shoreline, revealing areas of increased erosion ("hot spots") or areas of increased wave energy. These data then provide the basis for nearshore circulation and sediment transport models. In addition, one of the primary advantages of wave modeling is its ability to simulate multiple scenarios. The model domain can be modified (e.g., comparison of existing and post-dredging scenarios, different structural configurations, evaluation of varying beach nourishment templates, etc.) to determine the effect various changes have on the wave climate. Wave input also can be modified to simulate a wide range of wave conditions (e.g., storm events, seasonal variations) to determine changing impacts on shoreline response.

This section focuses on the application and results of wave transformation numerical modeling for offshore Alabama. A combined refraction and diffraction spectral wave model was used to propagate random waves from offshore to the nearshore region and investigate potential changes in the wave field caused by dredging of offshore borrow areas. The purpose of this section is to describe the framework and capabilities of the wave model, explain its application to the Alabama coastline, and provide analysis of the modeling results used as input to the numerical circulation and sediment transport models.

4.1.1 Wave Model Description

The spectral wave refraction/diffraction model REF/DIF S (Kirby and Özkan, 1994) was employed to evaluate changes in wave propagation across the Alabama continental shelf relative to potential sand mining scenarios. REF/DIF S is a combined refraction and diffraction spectral wave model, which can simulate the behavior of a random sea state and incorporates the effects of shoaling, wave breaking, refraction, diffraction, and energy dissipation. Using wave data collected in the Alabama coastal region, appropriate input can be developed and used to specify offshore wave boundary conditions. Then, using local bathymetry to create an accurate grid, the model is able to propagate waves to an area of interest (e.g., Dauphin Island, Gulf Shores). The following discussion provides a comprehensive description of the REF/DIF S, including a brief summary of the theoretical background.

Understanding water wave propagation over an irregular bathymetry can be improved greatly through the implementation of a spectral wave model rather than a monochromatic wave model. The use of a spectral wave model provides the capability to propagate all components of ocean waves simultaneously through the model domain. The spectral approach makes it possible to calculate

nearshore statistical wave parameters and represent the actual sea surface more accurately. Typically, ocean wave energy is composed of a large variety of waves moving in different directions and with different frequencies, phases, and heights. By simulating all wave components that propagate towards the Alabama shoreline, a spectral wave model is superior to a monochromatic wave model.

To illustrate the increased accuracy gained when using a spectral wave model, a comparison was made between spectral model results (REF/DIF S), monochromatic results (REF/DIF 1), and experimental data collected by Vincent and Briggs (1989) for waves propagating over a submerged shoal. The upper left-hand panel of Figure 4-1 illustrates bathymetry used in the experiments conducted by Vincent and Briggs (1989). The bottom panels present normalized wave height results for two (monochromatic and spectral) model simulations. The dashed black lines on the bottom two plots show contours of the submerged shoal, while the solid white lines are contours of normalized wave height (also presented as a color map). Both monochromatic (REF/DIF 1, lower left-hand panel) and spectral (REF/DIF S, lower right-hand panel) results illustrate wave focusing that occurs behind the submerged shoal; however, the monochromatic wave model tends to focus wave energy to a much greater degree than the spectral wave model. In addition, monochromatic wave model results show more "jagged" wave height patterns induced by the presence of the shoal.

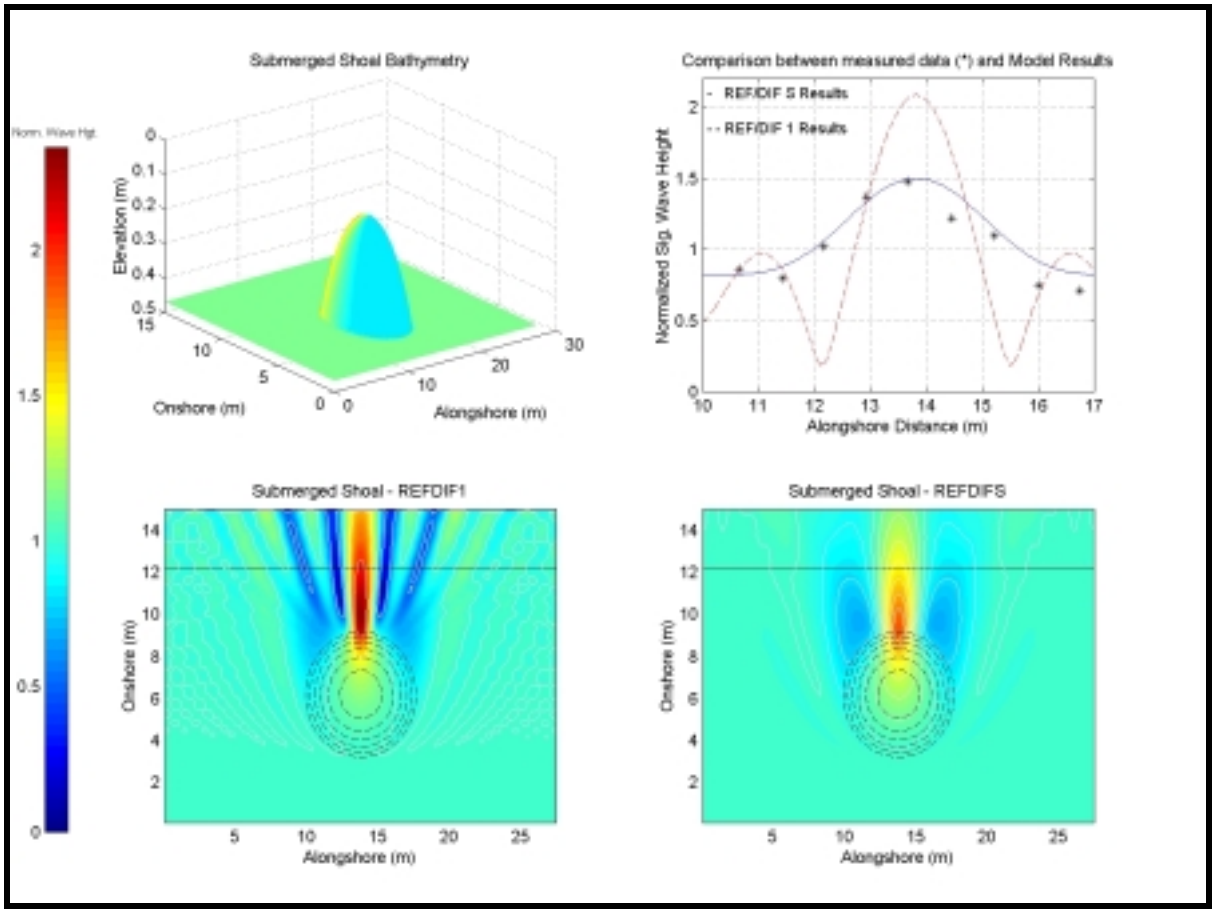

Figure 4-1. Comparison between a spectral (REF/DIF S) and monochromatic (REF/DIF 1) wave models. Wave height results are compared to measured data (*) collected by Vincent and Briggs (1989).

The upper-right hand plot shows a comparison between spectral model results (-), monochromatic model results (- -), and measured data (*) for a transect taken 12.2 m from the offshore boundary (indicated by the solid black line in the lower panel plots). Spectral wave model results compare well with the general shape of the curve depicted by the measured data, while monochromatic wave model results over-predict wave focusing and under-predict wave height on either side of the focusing.

REF/DIF S simulates the behavior of a random sea surface by describing wave energy density as a function of direction (directional spectrum) and frequency (frequency spectrum). The two-dimensional wave spectrum is discretized into separate wave components, which make up an essential part of the input for REF/DIF S. Therefore, at any point (*x,y*) in the model domain, water surface elevation is represented as

$$\eta(x,y,t) = \sum_{f}\sum_{\theta}\left\{\frac{A(x,y,f,\theta)}{2}e^{i\psi}\right\} \tag{4.1}$$

where $A(x,y,f,\theta)$ is the complex amplitude, f is the component's frequency, θ is the direction of any individual wave component, and

$$\psi = \int k \cdot dx - \omega t \tag{4.2}$$

is the phase of the wave component, k is the wave number, and ω is the radian frequency. The wave number vector, k, can be defined in terms of its components in the x and y directions and related to the direction of any individual wave component, θ_n, by:

$$k_x = k_n \cos\theta_n \tag{4.3}$$

$$k_y = k_n \sin\theta_n \tag{4.4}$$

Figure 4-2 shows the coordinate convention used in the present wave modeling study and the angle made by each wave component relative to the x-axis.

Input wave spectra are comprised of discrete, bin-centered values of frequency and direction specified at the offshore boundary. A description of the development of specific input conditions for the Alabama wave modeling grids is presented in Section 4.1.3. Computations in the model domain are performed simultaneously for all wave components, n. After each shoreward step in the model grid, the complex amplitudes, $A(x,y)_n$, are known for all wave components contained within the selected spectra. REF/DIF S calculates the significant wave height ($H_{1/3}$), based on all the components, as:

$$H_{1/3}(x,y) = \sqrt{8\sum_{n=1}^{N}\left|A(x,y)_n\right|^2} \tag{4.5}$$

where N is the total number of wave components and $A(x,y)_n$ is the complex amplitude of the wave component n. Historically, significant wave height, which is the average of the one-third highest waves, has been referenced for characterizing the sea state, and it is used throughout REF/DIF S in additional computations (e.g, wave breaking).

As waves propagate over irregular bathymetry, complex interactions between individual waves and other natural physical phenomena create modifications to the wave field that result in a complicated three-dimensional problem. REF/DIF S is a parabolic model that solves this complex problem based on the mild slope equation developed by Berkhoff (1972).

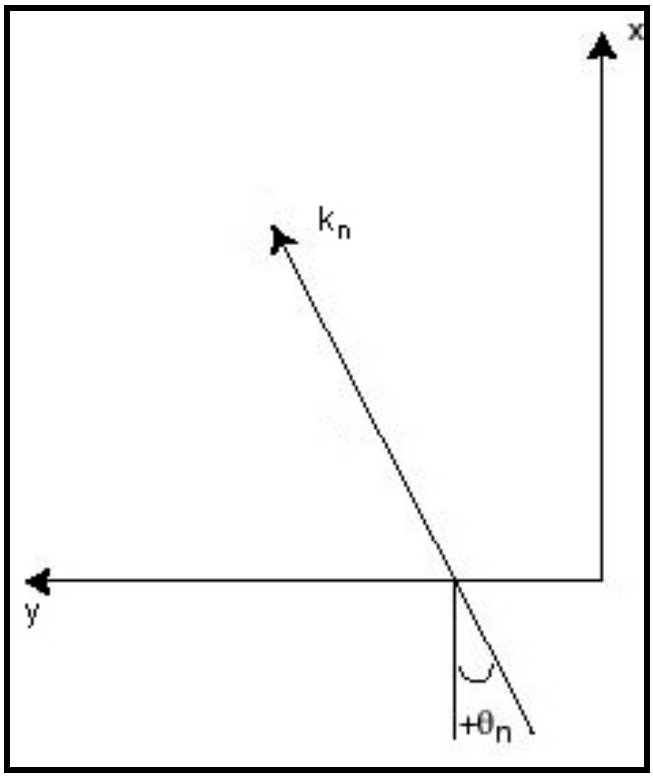

Figure 4-2. Coordinate and angle convention used for the wave modeling in the present study.

The vertically integrated mild slope equation can be written in terms of the horizontal gradient operator as:

$$\nabla_h \cdot (CC_g \nabla_h \eta) + k^2 CC_g \eta = 0 \tag{4.6}$$

where,

$$C = \sqrt{(g/k)\tanh kh} \quad \text{(Wave Celerity)} \tag{4.7}$$

$$C_g = C(1 + 2kh/\sinh 2kh)/2 \quad \text{(Group Velocity)} \tag{4.8}$$

and g = acceleration of gravity and h = local water depth.

Although the mild slope equation is an approximation, it is accurate in both deep and shallow water and is sufficient even for large local bottom slopes (Booij, 1983). REF/DIF S uses the linear form of the mild slope equation and includes the effects of shoaling, non-linear refraction and diffraction (Kirby, 1983; Kirby and Dalrymple, 1983a), wave breaking, energy dissipation, and wave-current interaction (Kirby, 1984; Kirby and Dalrymple, 1983b). Equation 4.9 presents the complete form of the revised mild slope equation.

$$\frac{\partial A_n}{\partial x} = \frac{i}{2k_n}\frac{\partial^2 A_n}{\partial y^2} - \frac{\omega_n}{2C_{gn}} A_n - \alpha A_n \tag{4.9}$$

where ω_n is the dissipation factor.

Through a combination of the various wave directions and frequencies, REF/DIF S is able to simulate the behavior of a random sea. In addition, detailed analysis and selection of input spectrum allows the model to assess the impact of different seasonal conditions and storms.

4.1.1.1 Refraction and Diffraction

Wave refraction and diffraction have a significant impact on wave transformation along the coast. Wave refraction (Figure 4-3) tends to align wave crests parallel to offshore depth contours and eventually the shoreline. Wave energy may be distributed unevenly along the coast; therefore, wave refraction results indicate potential variations in sediment transport pathways. Wave diffraction (Figure 4-3) tends to spread wave energy as a wave passes a structure or a shoal. This effect is most evident behind shore parallel breakwaters. As waves propagate past a breakwater, they bend towards the shadow zone behind the structure. Wave energy is then transferred along wave crests towards regions of smaller wave height. As with wave refraction, diffraction also will result in an uneven distribution of wave energy along the coast.

In some cases, refraction and diffraction occur simultaneously, and it is important to be able to simulate both phenomena. REF/DIF S simulates refraction and diffraction using a parabolic approximation developed by Radder (1979) and Lozano and Liu (1980) to solve the mild-slope equation. This parabolic model was further extended by Kirby and Dalrymple (1983a) to be weakly non-linear. Comparisons with laboratory data (Kirby and Dalrymple, 1984) show the importance of non-linear dispersion terms in the governing equations as the weakly non-linear model indicated better agreement with the observed laboratory data.

4.1.1.2 Energy Dissipation

In nature, sea floor characteristics vary from muddy substrates to sandy, rippled beds to rough, rocky bottoms. Therefore, assuming a rigid, impermeable horizontal seafloor is inadequate for quantifying wave transformation. To varying degrees, water waves are influenced by these bottom characteristics through wave damping. Energy dissipation is accounted for in REF/DIF S with three potential energy dissipation options assigned to the dissipation factor, ω_n, presented in Equation 4.9.

1. *Laminar Surface and Bottom Boundary Layers* - accounts for the damping associated with boundary layers caused by viscosity at the surface and bottom as

$$\omega_n = \frac{\sigma_n k_n \sqrt{(\nu / 2\sigma_n)}(1-i)}{\tanh k_n h} \quad \text{(Surface)} \tag{4.10}$$

$$\omega_n = \frac{2\sigma_n k_n \sqrt{(\nu / 2\sigma_n)}(1-i)}{\sinh 2k_n h} \quad \text{(Bottom)} \tag{4.11}$$

where σ_n is the frequency and ν is the kinematic viscosity.

2. *Turbulent Bottom Boundary Layer Damping* - accounts for wave conditions that result in a turbulent bottom boundary layer, as would occur in nature. The dissipation term is

$$\omega_n = \frac{2\sigma_n k_n f \left| A_n \right|}{3\pi \sinh 2k_n h \sinh k_n h} \tag{4.12}$$

where f represents the Darcy-Weisbach friction factor.

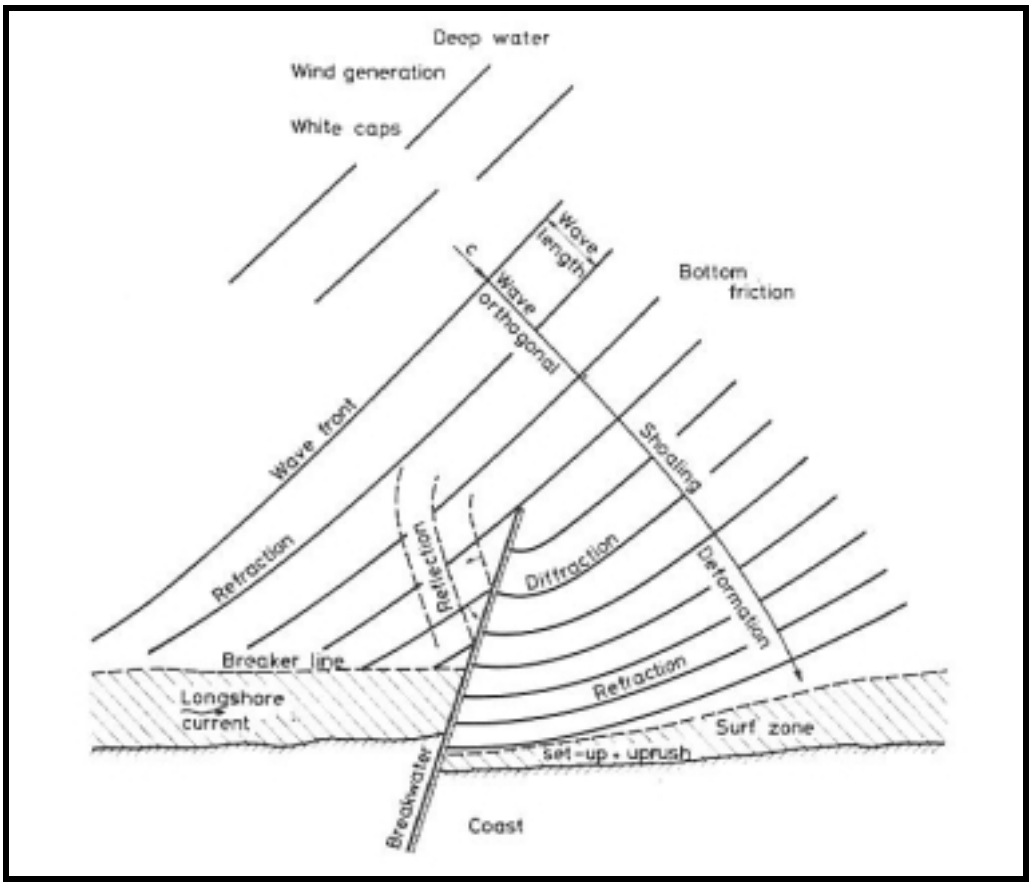

Figure 4-3. Diagram indicating the effects of refraction and diffraction as waves approach the coastline (from Svendsen and Jonsson, 1976).

3. *Porous Sand Damping* - accounts for wave damping due to the Darcy flow into sand bed where the dissipation term is

$$\omega_n = \frac{gk_nC_p}{\cosh^2 k_n h} \tag{4.13}$$

and C_p is the coefficient of permeability.

For this study, wave damping was simulated using a turbulent bottom boundary layer to most accurately represent natural conditions in the northeastern Gulf of Mexico. The assumed Darcy-Weisbach friction factor, *f*, in REF/DIF S is set equal to 0.01 by the model.

4.1.1.3 Wave Breaking

As a wave proceeds into shallow water, it continues to shoal and increase in wave height. However, at some depth, a wave will become unstable and break. Seafloor and wave characteristics determine how a wave will break. In REF/DIF S, the breaking model developed by Thornton and Guza (1983) is employed to dissipate energy in the form of turbulence. Energy dissipation is expressed as:

$$-\varepsilon_b = \frac{\partial EC_{gn}}{\partial x} \tag{4.14}$$

where energy, *E,* is expressed as

$$E = \frac{1}{8}\rho g H_{rms}^2 \tag{4.15}$$

and bore dissipation, ε_b, is

$$\varepsilon_b = \frac{3\sqrt{\pi}}{16}\frac{\rho g f_p B^3}{\gamma^4 h^5} H_{rms}^7 \tag{4.16}$$

In Equation 4.16, f_p is the peak spectral frequency, $H_s = 1.41 H_{rms}$, and B and γ are constants equal to 1 and 0.6, respectively. The breaking coefficient, α, as presented in Equation 4.9, is a function of the bore dissipation and is very small when breaking does not occur. However, once breaking starts, α begins to take on significant values and energy is dissipated from the wave field.

$$\alpha = \frac{4\varepsilon_b}{\rho g H_{rms}^2} \tag{4.17}$$

4.1.1.4 Radiation Stresses

After each forward computational step, REF/DIF S calculates radiation stresses for waves propagating at angle θ and outputs the values at every grid point in the model domain. For spectral modeling, radiation stresses are computed as a summation over all of the spectral wave components. Radiation stress in the y-direction due to the excess momentum flux in the x-direction is given by

$$S_{xy}(x,y) = \frac{1}{4}\rho g \sum_{n=1}^{N}\left(\frac{C_{gn}}{C_n}\right)(x,y)\left|A(x,y)_n\right|^2 \sin 2\theta(x,y)_n \tag{4.18}$$

Likewise, radiation stress in the x-direction due to the momentum flux in the x-direction and radiation stress in the y-direction due to the momentum flux in the y-direction are given by:

$$S_{xx}(x,y) = \frac{1}{2}\rho g \sum_{n=1}^{N}\left|A(x,y)_n\right|^2\left\{\left(\frac{C_{gn}}{C_n}\right)(x,y)(1+\cos^2\theta(x,y)_n) - \frac{1}{2}\right\} \tag{4.19}$$

$$S_{yy}(x,y) = \frac{1}{2}\rho g \sum_{n=1}^{N}\left|A(x,y)_n\right|^2\left\{\left(\frac{C_{gn}}{C_n}\right)(x,y)(1+\sin^2\theta(x,y)_n) - \frac{1}{2}\right\} \tag{4.20}$$

respectively. Radiation stress results are used as input to the nearshore circulation model and sediment transport simulations.

4.1.1.5 Subgrids

Another feature of REF/DIF S is its capability to use a coarse-scale (typically hundreds of meters) reference grid and a fine-scale subgrid, which can have many times the resolution of the reference grid. The subgridding option can be implemented to resolve important topographic features (e.g., artificial islands, shoals, borrow pits, etc.) or increase resolution for coupling with

additional models (e.g., nearshore circulation). Figure 4-4 illustrates a case where a subgrid becomes important to increase resolution at a sand borrow site. The selection and development of reference grids and subgrids for the present study can be found in Section 4.3.

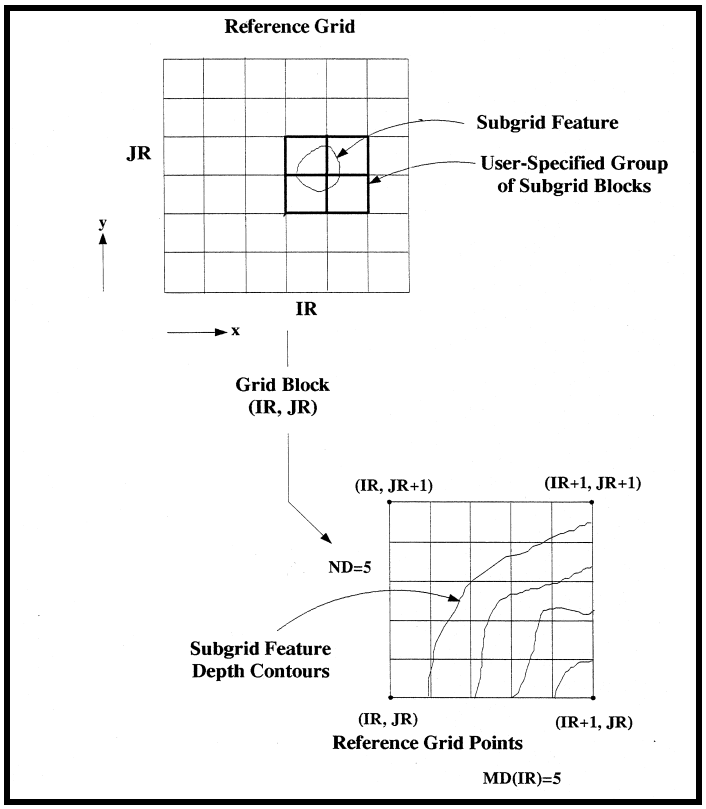

Figure 4-4. Example of subgrid development over a borrow pit feature (Kirby and Özkan, 1994).

4.1.2 Required Input Conditions

Wave modeling requires an offshore wave specification and a bathymetric grid. By analyzing collected offshore wave data (National Oceanic and Atmospheric Administration [NOAA] wave buoys as well as other sources) or USACE WIS hindcast wave data, the appropriate wave input (spectra) can be developed and used to specify the offshore forcing boundary condition. By using local bathymetry to create an accurate grid, determine lateral boundary conditions, and select appropriate dissipation parameters, the model is capable of propagating waves to the area of interest. A comprehensive description of wave characteristics and spectral input determination can be found in Section 4.2, while development of site-specific reference grids (both existing and post-dredging) for the Alabama wave transformation numerical modeling can be found in Section 4.3.

4.1.3 Wave Model Limitations and Modifications

The version of REF/DIF S used in this study was modified from REF/DIF S version 1.2 and obtained from Dr. James Kaihatu of the Naval Research Laboratory, Oceanographic Division at the Stennis Space Center, Mississippi. Dr. Kaihatu discovered limitations in the calculation method of the wave group velocity in REF/DIF S, which constrained the selection of y-subdivisions to the value of one. He also updated the finite difference scheme used for calculating peak wave approach angle, as well as disabled the internal, numerical filtering mechanism to reduce energy loss from the wave field. The removal of numerical filtering eliminated alongshore smoothing.

Additional modifications were made to REF/DIF S for the present study. The limitation discovered in the calculation of wave group velocity was corrected, allowing an uninhibited selection of y-subdivisions. The number of y-subdivisions can become critical depending on reference model grid spacing and bathymetric changes in the model domain. The ability to increase the number of alongshore subdivisions improves model resolution in the alongshore direction and allows more accurate calculation of wave field characteristics. REF/DIF S also was upgraded to run in either monochromatic or spectral modes, to allow for larger reference grids and subgrids, and to provide user-controlled output of major parameters (i.e., wave height, radiation stresses, etc.) within subgrid regions.

Although more advanced wave models are currently under development (i.e., Bousinesq modeling), the wave modeling presented here is similar to other currently accepted spectral wave modeling techniques and is adequate for gauging potential changes in the wave field caused by offshore sand mining. However, wave prediction capabilities are still limited even when using the spectral approach. Required computation time limits the spectral representation to discrete bins in the directional and frequency domains. Simulation of a continuous spectra, rather than discrete bins, would yield a more comprehensive and accurate representation of the wave field. In addition, REF/DIF S does not define the peak angle approach well in directional, multi-component seas or when waves become short crested. Wave modeling also requires detailed input (wave fields and bathymetric information) to produce high quality results, specifically those required to drive nearshore circulation and sediment transport models.

Existing modeling techniques also may be limited for simulating long-period, high-energy wave events (or storms), and the accuracy of results for these simulations is questionable. The reduced number of spectral components used for simulating long-period, high-wave events, as well as the lack of internal alongshore energy dispersion, produce wave modeling results with substantial gradients in alongshore wave height. These gradients (or streaks) associated with long wave period events indicate the limitation of REF/DIF S for areas with highly-variable offshore bathymetric contours, such as the eastern Alabama shelf. For these cases, REF/DIF S tends to over-predict wave focusing.

Despite some of the limitations of spectral wave modeling, it is the best overall technique currently available to simulate wave propagation. REF/DIF S is capable of accurately simulating most wave fields, and it is efficient for identifying potential modifications to the wave field caused by offshore sand mining.

4.2 WAVE CHARACTERISTICS AND INPUT SPECTRA

A key component of accurate wave modeling is the analysis and selection of input wave data. The results derived from numerical wave transformation modeling are controlled by the quality of selected input data and parameters. This section describes the analysis and selection of input wave parameters for the modeling effort and focuses specifically on the development of seasonal and extremal spectra.

4.2.1 Wave Data Analysis and Sources

4.2.1.1 Wave Information Study and NOAA Buoy Data

The U.S. Army Corps of Engineers Wave Information Study (WIS) has met a critical need for wave information in coastal engineering studies since the 1980s. WIS contains time series information of spectrally-based, significant wave height, peak period, peak direction, and wind speed and direction produced from a computer hindcast model. The hindcast wave model, WISWAVE (Resio and Tracy, 1983), is run using wind data (speed and direction) at selected coastal locations around the United States. The model provides wave climate based on local/regional wind

conditions. Because the data are numerically generated, consistent and long-term wave data are available at most coastal locations. WIS data used in this study include the effects of storms; however, the effects of extreme events, such as hurricanes, are not included. Simulation of an extreme, high energy event for the study area is incorporated using extremal analysis. WIS information originally was calculated by hindcasting deepwater waves from historical surface pressure and wind data (Brooks and Corson, 1984). The Phase I-type model used large-scale atmospheric conditions, a large grid size (hundreds of kilometers), and only one type of wave process, air-sea interaction. Phase I results do not include such effects as shoaling, bottom friction, or long waves. Although simplifications are present in Phase I-type modeling, it still provides adequate approximations of time-series results.

Wave measurements made by the NOAA during the 1980's made verification of WIS results possible by comparing the statistics and the distributions of wave heights and periods from different time periods (Hubertz et al., 1993). Improvements have been made through subsequent modeling efforts to increase the accuracy of WIS relative to NOAA measurements. Phase II-type WIS data, which include the effects of shoaling, refraction, diffraction, and bottom friction, were used in the present study. The Phase II WIS data provide wave parameter results every three hours.

The availability and long-term records make WIS information attractive when considering average or seasonal wave conditions. Since the data are widespread and continuous, adoption of the WIS data for development of spectral wave conditions is applicable. WIS stations used are located at or near the offshore boundary of the wave transformation model grid. Table 4-1 provides a summary of the WIS stations used in the present spectral wave modeling effort along the Alabama coast.

Table 4-1. Summary of relevant WIS stations in the modeling domain.

WIS Station	G1046	G1047
Reference Grid	B (Resource Areas 1, 2, & 3)	A (Resource Areas 4 & 5)
UTM Northing (m)	3,318,842	3,319,262
UTM Easting (m)	427,661	403,547
Depth (m)	28	28
Time Period (yrs)	1976 to 1995	1976 to 1995

Each of these stations is located seaward of the five sand resource areas in 28-m water depth. Input data (energy and directional spectra) for the reference grids are developed from simulated wave data for these two stations. Wave parameters do not differ significantly between the two stations. However, due to the significant distance between the two modeling grids, input spectra are generated for each grid separately.

Another source of wave data readily available in the Gulf of Mexico is NOAA observed wave data. The benefit of using NOAA data is that it is measured rather than hindcasted (predicted). Therefore, it includes high energy events, such as hurricanes. However, because NOAA buoys are collecting actual observations, the buoys are subject to severe weather and mechanical problems, and therefore, a consistent long-term wave record is more difficult to attain. Table 4-2 presents the locations and availability of NOAA data for offshore Alabama. The observed data consist of numerous gaps, limited deployment times, and changes in deployment location. These variables resulted in an incomplete and unfavorable wave data set. For example, directional wave data were collected only during time periods when the NOAA buoys were deployed landward of the sand resource areas (Table 4-2). Only during a brief deployment (Buoy 42015, December 1987 to December 1988) were wave data collected seaward of the sand resource areas. Spatial and

temporal data limitations made it difficult to use NOAA observations for anything more than ancillary data.

Table 4-2. Inventory of relevant NOAA stations in the modeling domain.

Station ID	Location	Deployment Time	Wave Data	Wind Data	Wave Direction
42015	30.1 N / 88.2 W	4/87-8/87 9/87-10/87 11/87 12/87-12/88	O O O X	X X X X	O O O X
42015	30.2 N / 88.2 W	12/88-9/90	X	X	X
42016	30.2 N / 88.1 W	4/88-9/88 9/88-12/88 4/89-11/89 2/90-5/90 7/90 8/90-9/90	X X X X X X	X X X X X X	X X X X O X
42016	29.9 N / 88.0 W	12/93-1/94 2/94-3/95	O O	X X	O O
42016	30.2 N / 88.2 W	5/95 6/95	O O	X X	O O

X = data collected; O = no data collected

4.2.1.2 Data Comparison

In order to verify the accuracy of WIS hindcast data used in this study, a comparison was made between hindcast data and a time period (December 1987- December 1988) when wave data (NOAA Station 42015) were collected at approximately the same location. Figure 4-5 presents the results of the comparison from two distinct time periods in 1988 (January through April and May through September). Although differences exist between the data sets, WIS information simulates the structure and peaks of observed wave data fairly well. For the time period when WIS and NOAA data were available at similar locations (approximately one year), observed wave heights were within ±0.25 meters approximately 70% of the time, and within ±0.5 meters 93% of the time. The observed wave periods were within ±1 second of the hindcast data 72% of the time, and within ±2 seconds 96% of the time. A comparison of wave directions was not performed since the measured NOAA data did not include directional information during this deployment interval. Based on the results of the comparison, it was determined that the WIS data set was adequate for developing seasonal wave input conditions.

4.2.1.3 Seasonal Characteristics

A detailed understanding of local wave climate is required to produce representative wave modeling simulations. The 20-yr (1976-1995) WIS data offer a synopsis of the wave climate offshore Alabama. An examination of local WIS stations (G1047 and G1046) provides a detailed description of the wave climate and development of appropriate input spectra.

Rather than selecting the most common wave heights and directions, a detailed analysis was conducted to summarize existing WIS data into average seasonal wave conditions and spectra. Each season may contain distinct differences in energy and/or directional spectra, and consequently produce varying impacts at borrow locations. Simulation of seasonal characteristics (averaged over 20 years) provides a method to identify these changes. For example, if there is a difference in mean

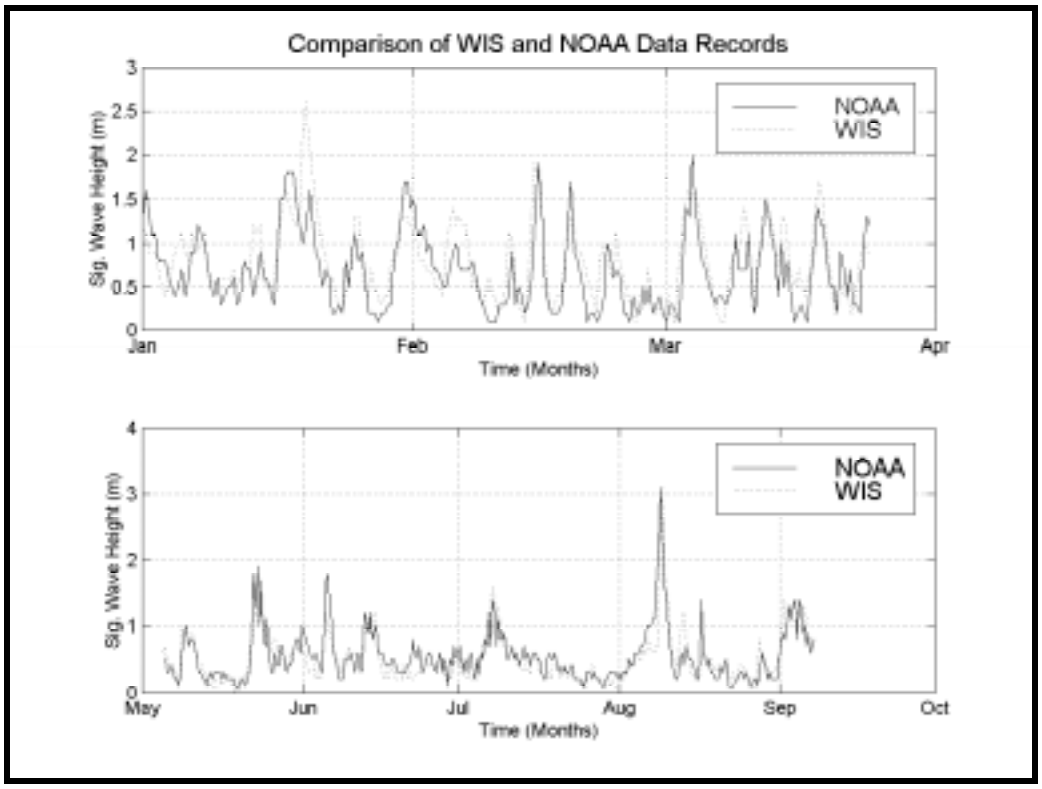

Figure 4-5. Comparison of WIS hindcast (dotted) and NOAA observed (solid) significant wave height for two time periods in 1988.

direction of wave approach during the summer and winter seasons, simulations for these two seasons may result in varying impacts caused by removal of sediment from potential borrow sites. Also, averaging 20 years of wave data creates typical seasonal wave conditions offshore Alabama. Spectra developed for the Alabama shoreline indicate that all seasonal waves propagate from east-to-west. Therefore, seasonal spectra do not incorporate the effects of occasional reversals in wave direction.

To summarize the historical data into appropriate seasons by energy and directional spectra, monthly wave conditions were examined for each WIS station. Figures 4-6 through 4-9 present examples of the monthly breakdown conducted using historical data. Figure 4-6 shows histograms of peak wave period and associated direction for the month of May, averaged over 20 years (1976 to 1995) for Station G1046 (Grid B). Figure 4-7 presents similar plots for the month of November. The analysis uses a high frequency cut off of 0.2 Hertz (5 sec) to eliminate periods of low wave energy from the analysis. Although wave components with periods less than 5 sec do contribute to the wave field, they do not contribute significantly to the sediment transport analysis. Wave periods of less than 5 seconds would require a higher resolution model grid, which would substantially increase model simulation time. Due to the extensive region evaluated, as well as the negligible impact to sediment transport calculations, wave periods less than 5 seconds were excluded from the analysis. During the month of May, the direction of wave approach is concentrated around a primary direction (narrow spreading), while during the month of November, an increase in spreading is evident. Also, greater low frequency (high period) waves appear during November than May. These differences illustrate the importance of evaluating specific seasonal phenomena rather than focusing only on overall average conditions.

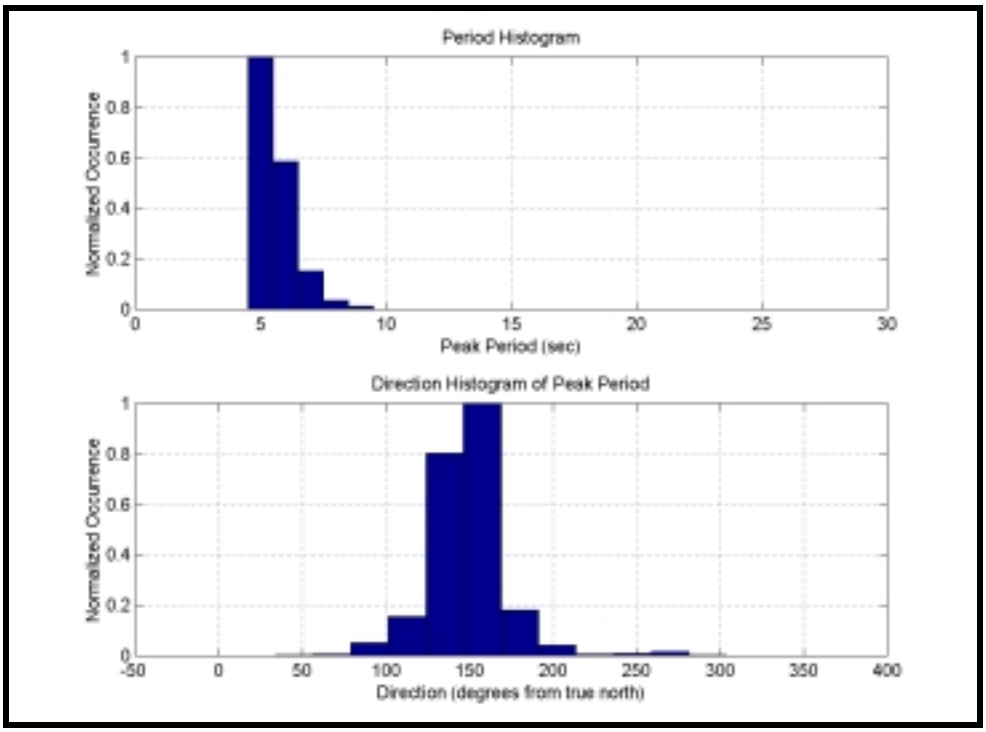

Figure 4-6. Histogram plots of 20-yr averaged peak periods and associated wave directions for the month of May at WIS Station G1046. The vertical bars are normalized by the greatest occurrence bin.

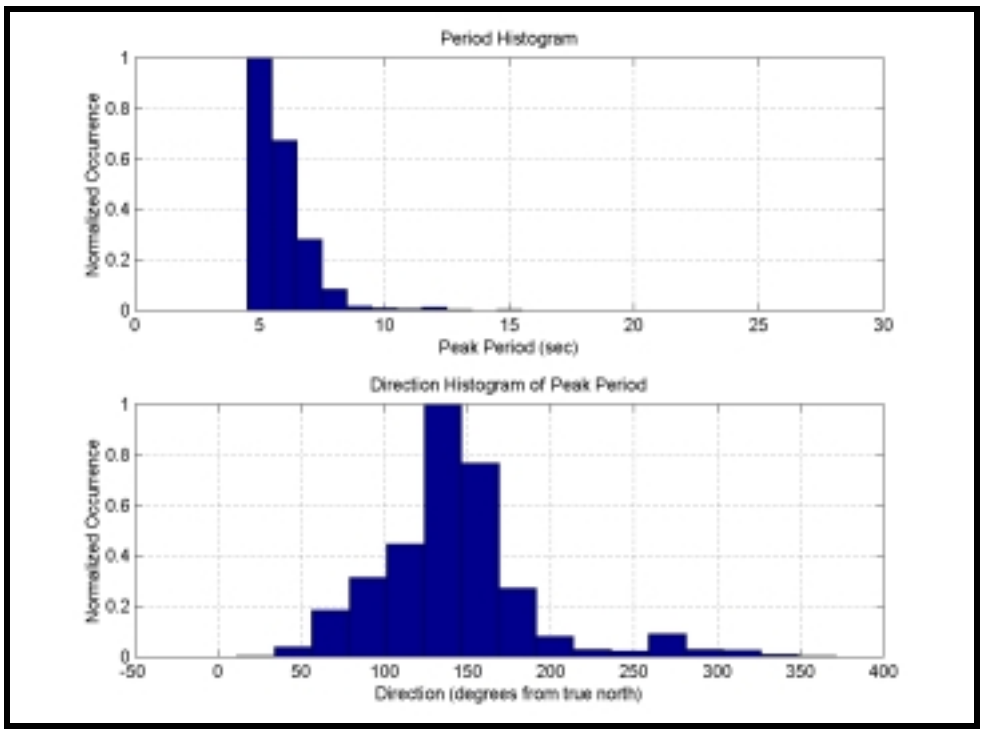

Figure 4-7. Histogram plots of 20-yr averaged peak periods and associated wave directions for the month of November at WIS Station G1046. The vertical bars are normalized by the greatest occurrence bin.

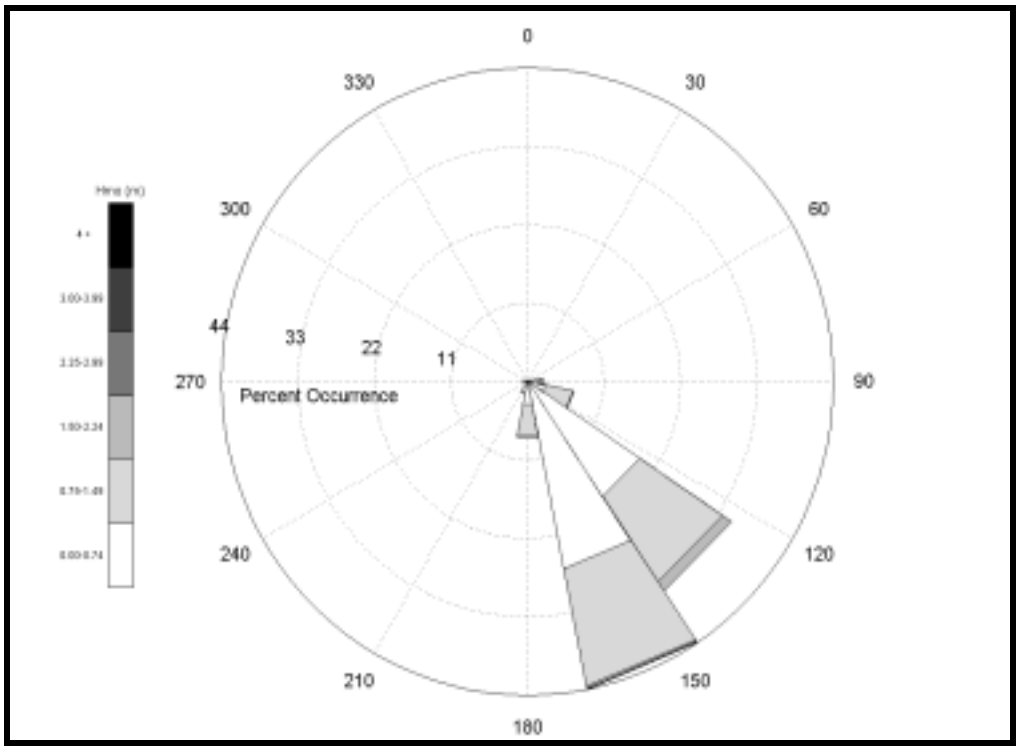

Figure 4-8. Twenty-year averaged wave rose for May at WIS Station G1046.

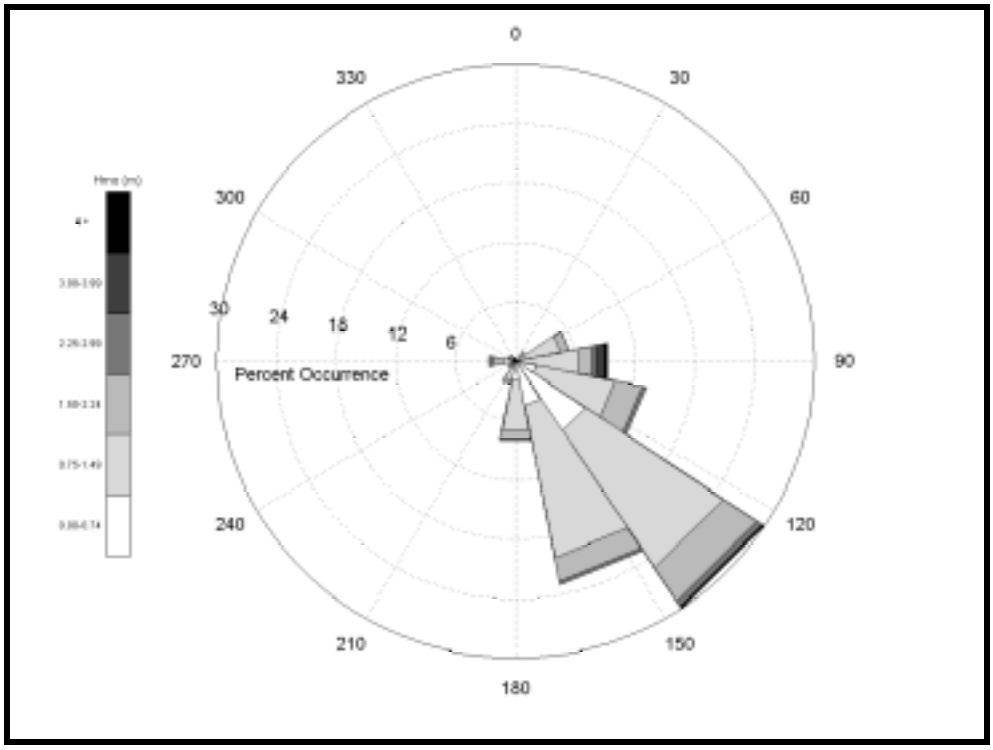

Figure 4-9. Twenty-year averaged wave rose for November at WIS Station G1046.

The distribution of significant wave height data (illustrated using a wave rose plot) for the months of May and November is presented in Figures 4-8 and 4-9, respectively. The color scale indicates the magnitude of wave height, the circular axis represents the direction of wave approach (coming from) relative to North (0 degrees), and the extending radial lines indicate percent occurrence within that magnitude and directional band. The month of November consists of higher energy waves and, as indicated with the directional spread of energetic wave periods (Figure 4-9), greater directional spreading. In contrast, the month of May has smaller wave heights and less directional spreading. Similar average breakdowns were completed for both WIS stations and all months.

Evaluation of wave characteristics for individual months provided a breakdown of the data set into specific seasonal averages. Using statistical summaries of monthly wave data (i.e., mean significant wave height, standard deviation of the significant wave height, mean direction, mean peak period, etc.), as well as the visual summary of data presented above, average seasons were determined. Monthly data were grouped by similar wave conditions (i.e., wave height, directional spread, frequency distribution, etc.) to form representative wave seasons and provide a convenient way to delineate the changes in wave climate. For example, summer seasons may be characterized by smaller wave heights and shorter wave periods, while winter seasons may consist of larger waves with longer periods. Table 4-3 presents the seasonal breakdown for each of the WIS stations. Due to the reduced wave climate in the Gulf of Mexico, seasonal variability is not quite as evident as it is along many open ocean coastlines.

Table 4-3. Summary of the seasonal breakdown of the 1976-1995 WIS data.

WIS Station	G1046	G1047
Winter	December to February	December to February
Spring	March to May	March to May
Summer	June to August	June to August
Fall	September to November	September to November

Following the seasonal delineation, frequency and directional histograms, as well as wave rose plots, were developed for the four seasons. For example, Figure 4-10 presents the peak period and associated directional histograms for the spring season extracted from Station G1046. Figure 4-11 presents the wave height distribution in a wave rose for the same spring season. As before, the color scale indicates the magnitude of wave height, the circular axis represents the direction of wave approach (coming from) relative to North (0 degrees), and the extending radial lines indicate percent occurrence within that magnitude and directional band.

The recasting of WIS data into seasonal wave conditions was used in the development of energy and directional input spectra for REF/DIF S. A more detailed discussion on the development of individual seasonal spectra can be found in Section 4.2.2.1.

4.2.1.4 High Energy Events

As discussed in Section 4.2.1.1, WIS data used in this study do not include hurricanes. Since these high energy events have a significant impact on many physical processes (and in most cases, dominate sediment transport), it is crucial to include storm simulations in wave modeling to assess their impact of potential borrow sites. Therefore, high energy events are simulated using wave transformation modeling, in addition to evaluating average seasonal conditions.

High energy events were evaluated by reviewing existing literature on hurricanes in the Gulf of Mexico, investigating the storm tracks, and using an extremal-value approach to analyze historical data sets. Results of the analysis, coupled with historical storm tracks and wave directions, were used to determine wave heights, directions, and frequencies for simulating a high-energy wave

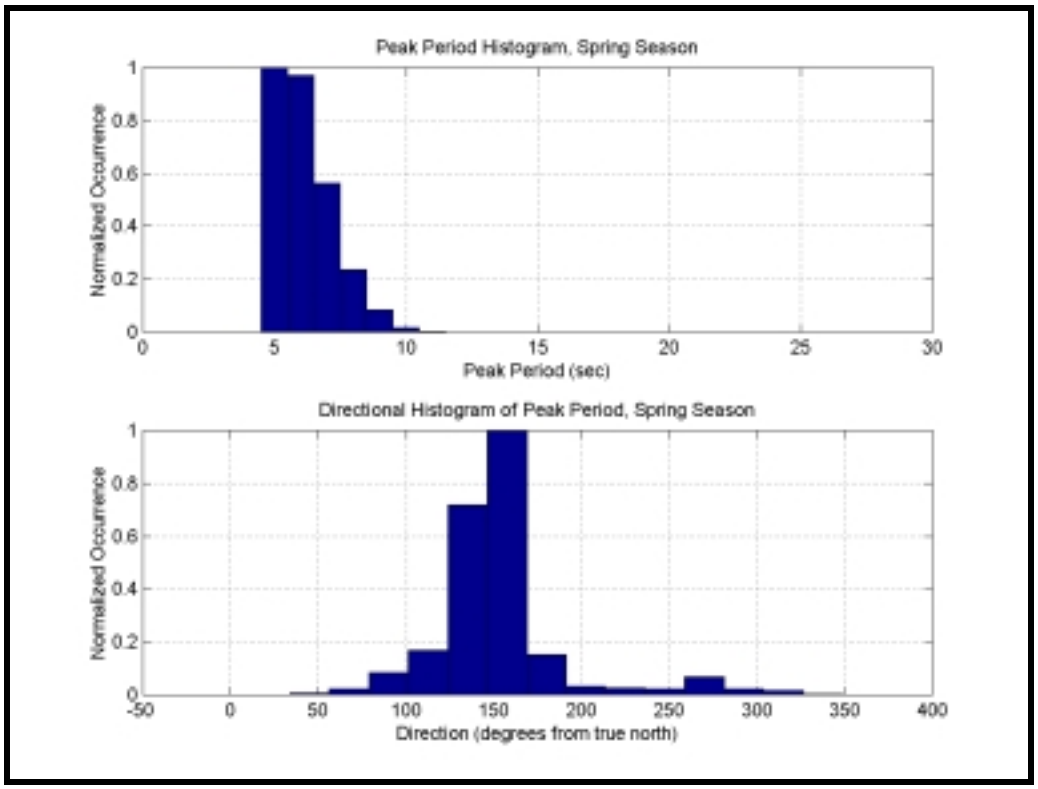

Figure 4-10. Histogram plots of 20-yr averaged peak periods and associated wave directions for the spring season at WIS Station G1046. Vertical bars are normalized by the greatest occurrence bin.

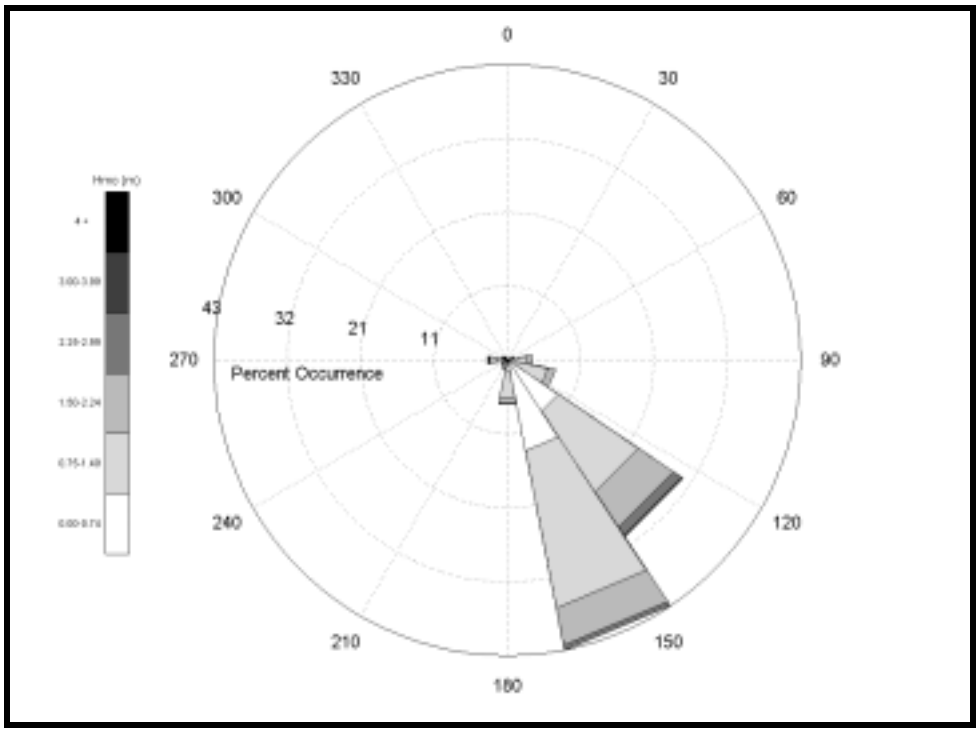

Figure 4-11. Twenty-year averaged wave rose for the spring season at WIS Station G1046.

event. Murray (1970) measured bottom currents near the coast during Hurricane Camille and also presented the track of the hurricane as it approached Gulf Shores. More recently, directional wave spectra observed during the passage of a frontal storm in the Gulf of Mexico were evaluated by Van de Voorde and Dinnel (1998).

Table 4-4 presents return periods calculated by the Coastal Hydraulics Laboratory (CHL), formerly the Coastal Engineering Research Center (CERC), based on WIS data (1976-1995). The return period can be thought of as the average period of waiting between events exceeding some specified value. Generally, return values are presented for 10 years, 25 years, 50 years, and 100 years, although any arbitrary return period can be calculated. The return periods calculated here are 2, 5, 10, 20, 25, and 50 years. For instance a 20-yr return value for a wave height of 6.4 m means that for any given year, there is a 1/20 chance that waves of 6.4 m will be reached. However, the return period is not the same as the probability that an event of a specific size will occur within a interval of time. Nor is the return period the frequency of occurrence of events of a given intensity. The specific selection of parameters representing the high energy (or extreme) wave event can be found in Section 4.2.3.

Table 4-4. Return periods based on the 1976 to 1995 WIS data.

Return Period (yr)	Significant Wave Height (m)	
	Station G1046	Station G1047
2	4.14	4.17
5	5.10	5.19
10	5.76	5.90
20	6.40	6.58
25	6.60	6.79
50	7.22	7.46

4.2.2 Seasonal Condition Parameters

4.2.2.1 Spectra Development

REF/DIF S requires input of a directional wave spectrum, which represents the distribution of wave energy in the frequency and direction domains. The two-dimensional spectrum is given as the product of the energy and directional spectra as:

$$S(f,\theta) = E(f)D(\theta) \tag{4.21}$$

where $S(f,\theta)$ is the directional wave spectral density function, $D(\theta)$ is the directional spreading function, and $E(f)$ is the frequency spectra. The directional spreading function provides the relative magnitude of directional spreading of wave energy, while the frequency spectra provides the absolute value of wave energy density.

Numerous empirical approximations have been developed to represent frequency and directional distributions. The frequency distribution for fully developed wind waves was approximated by Bretschneider (1968), or for deep water swell the JONSWAP formulation may be applied (Hasselmann et al., 1973). More recently, the TMA spectrum (Hughes, 1984) was developed for finite depths and is utilized in the present study. The TMA spectrum is given by the energy density, $E(f)$, for frequency f as:

$$E(f) = \frac{\alpha g^2}{(2\pi)^4 f^5} \exp\left\{-1.25\left(\frac{f_m}{f}\right)^4 + (\ln\gamma)\exp\left[\frac{-(f-f_m)^2}{2\sigma^2 f_m^2}\right]\right\}\phi(f,h) \tag{4.22a}$$

where α = Phillips' constant
f_m = peak frequency
γ = peak enhancement factor

The shape parameter, σ, is defined as

$$\sigma = \begin{cases} \sigma_a = 0.07 & \text{if } f < f_m \\ \sigma_b = 0.09 & \text{if } f \geq f_m \end{cases} \tag{4.22b}$$

The factor $\phi(f,h)$ incorporates the effect of depth on the frequency distribution by

$$\phi = \begin{cases} 0.5\left[\omega_h^2\right] & \text{if } \omega_h < 1 \\ 1 - 0.5\left(2 - \omega_h\right)^2 & \text{if } 1 \leq \omega_h \leq 2; \quad \omega_h = 2\,\pi\, f\,\sqrt{\dfrac{h}{g}} \\ 1 & \text{if } \omega_h > 2 \end{cases} \tag{4.22c}$$

where h = water depth.

The peak enhancement factor, γ, can be manipulated to represent the narrowness (or broadness) of the input frequency spectra. A narrow frequency spectrum means the waves in the wave group have a relatively compressed frequency range, while broad spectra contain waves ranging over a greater frequency distribution.

In a similar manner, the directional spreading distribution can be represented through various formulations. Borgman (1985) developed the following relationship, which is applied in the current study:

$$D(\theta) = \frac{1}{2\pi} + \frac{1}{\pi}\sum_{j=1}^{J} \exp\left[-\frac{(j\sigma_m)^2}{2}\right]\cos j(\theta - \theta_m) \tag{4.23}$$

where
θ_m = the mean wave direction
J = the number of terms in the series
σ_m = the directional spreading parameter

The directional spreading parameter, σ_m, can be selected to produce narrow or wide directional range. A broad directional spectrum identifies waves approaching the coast from many different directions, whereas a narrow directional spectrum centers the wave group around the primary wave direction.

4.2.2.2 Selection of Wave Conditions

Using the frequency distribution and directional spreading from WIS data, energy and directional spectra are generated to represent each seasonal scenario. WIS data distributions are matched with TMA frequency and directional spreading functions to obtain a best-fit of the data. The matching procedure involves adjustment and optimization of the peak enhancement factor and directional spreading parameter, as well as appropriate bin selection and energy conservation. After approximating the data with continuous and appropriate spectra, representative discrete components (in frequency and directional domains) are selected by discretizing the continuous spectra into energy conserving bins. Each component is representative of an energy conserving bin (equal area under the continuous curve).

Figure 4-12 illustrates the matching of spectra to spring season data at Station G1047 (Grid A). The upper two panels present the directional spreading verification (left-hand side) and the discretization of the continuous directional spreading function (right-hand side). The normalized amplitude histogram shows the directional distribution of WIS data (over 20 years) at Station G1047 during the spring season (Section 4.2.1.3). The triangles on both plots identify the discrete directional components representing continuous directional spectra. More spectral influence is placed at locations along the distribution where occurrences are more frequent. In this case, nine directional bins are used and the spreading is skewed slightly towards the negative direction of wave approach (southeast). Due to the directional limitation imposed in forward propagating wave models, a minimal portion of the directional energy may be lost for wide directional spreading. The lower two panels in Figure 4-12 present the frequency spectra verification (left-hand side) and the discretization of the continuous TMA spectrum function (right-hand side). As in the upper panels, the normalized amplitude histogram shows the frequency distribution of the WIS data (over 20 years) at Station G1047 during the spring season. The triangles on both plots identify the discrete directional components representing the continuous energy spectra. The cutoff frequency is evident in the derived spectra at 0.2 Hertz (5 sec). Again, discrete components are placed based on the makeup of each individual season while maintaining energy conservation. Nine components are used to divide the frequency spectra for the spring season.

As a second example, Figure 4-13 presents the matching of the spectra to the summer season data at WIS Station G1046 (Grid B). In this case, the energy and directional spectra are very narrow. Similar figures for all seasons and stations can be found in Appendix B1.

Following generation of the energy and directional spectra, values are coupled to produce discrete wave components forming a comprehensive seasonal wave group. For example, ten frequency bins and ten directional bins produces a wave field consisting of 100 individual waves. Tables 4-5 and 4-6 present a season-by-season summary of the spectral parameters used to develop input conditions corresponding to Grid A and Grid B, respectively. The parameters are used to develop the seasonal input wave conditions at the offshore boundaries.

4.2.3 High Energy Event Parameters

As an extreme simulation, a 50-yr storm event is modeled using the analysis presented in Section 4.2.1.4. Extremal wave heights were determined from return period calculations performed by the Army Corps of Engineers Coastal Hydraulics Laboratory (CHL). These calculations were based on WIS data from 1976 to 1995 at Stations G1046 and G1047. The corresponding storm event wave period was determined using the following equation:

$$T = 12.1\sqrt{\frac{H_o}{g}} \tag{4.24}$$

as presented in the Shore Protection Manual (US Army Corps of Engineers, 1984).

Directional and energy spectra are estimated for the 50-yr event through comparisons of previous storm spectra (Van de Voorde and Dinnel, 1998) and application of Borgman's (1985) spreading function and a TMA spectra, respectively. The observed spectra (Van de Voorde and Dinnel, 1998) are used for comparison purposes only because the 50-yr storm does not represent a specific hurricane or storm event. Tables 4-5 and 4-6 present the spectral parameters used to develop the 50-yr storm input conditions corresponding to Grids A and B.

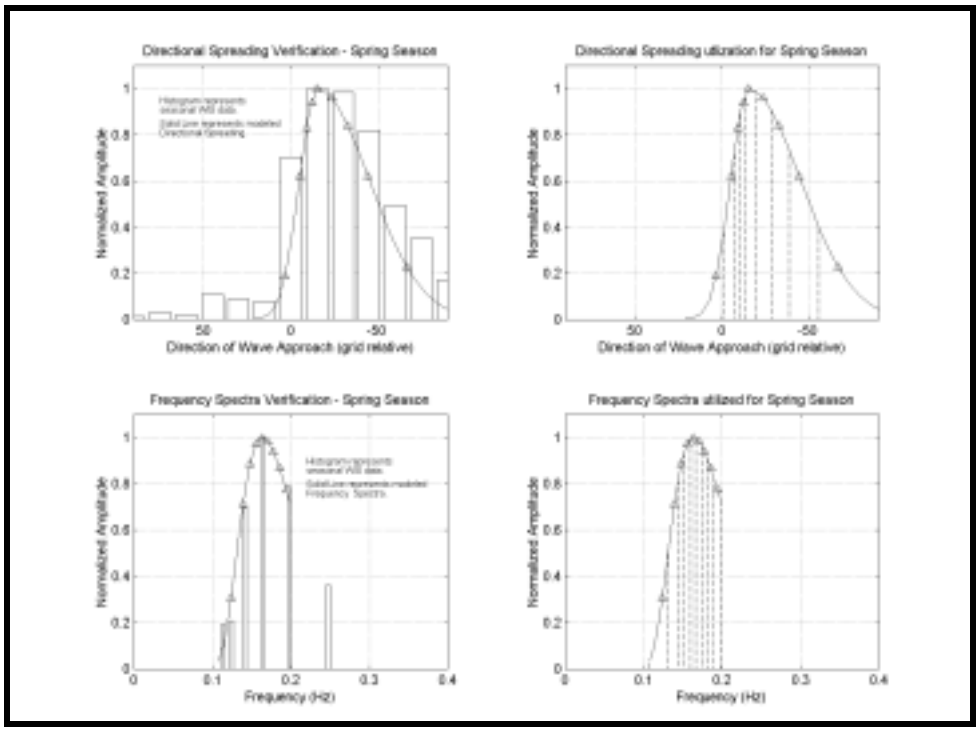

Figure 4-12. Energy and directional spectra verification and input set-up for the spring season at WIS Station G1047 (Grid A).

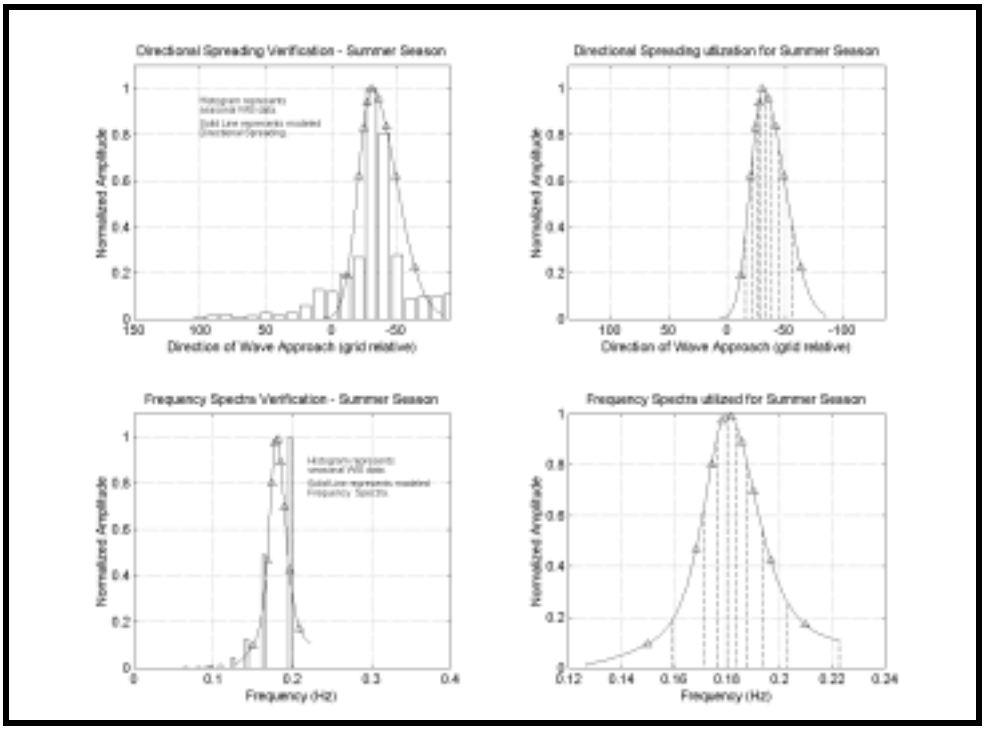

Figure 4-13. Energy and directional spectra verification and input set-up for the summer season at WIS Station G1046 (Grid B).

Table 4-5. Wave transformation numerical modeling input conditions and scenarios for Grid A (Dauphin Island)												
Scenario	Y-Sub	Spectra Type	# of E Bins	# of θ Bins	$T_{1/3}$	f_p	f_{max}	$\sigma_{m\ (+)}$	$\sigma_{m\ (-)}$	γ	H_s (m)	θ_m (grid relative)
Spring (Significant)	10	TMA	9	9	6.76	0.160	0.20	10	30	1.0	1.56	15°
Summer (Significant)	10	TMA	7	9	6.14	0.167	0.23	35	25	2.0	1.36	45°
Fall (Significant)	10	TMA	9	9	6.68	0.21	0.3	25	40	1.0	1.82	45°
Winter (Significant)	10	TMA	10	11	6.60	0.185	0.3	12	30	1.0	1.70	10°
50-yr Storm	10	TMA	7	5	10.6	0.095	0.125	5	5	1.0	7.46	5°
γ = Directional Peak Enhancement Factor (adjusted to fit seasonal spectra) σ_m = Directional Spreading Parameter												

Table 4-6. Wave transformation numerical modeling input conditions and scenarios for Grid B (Morgan Peninsula)												
Scenario	Y-Sub	Spectra Type	# of E Bins	# of θ Bins	$T_{1/3}$	f_p	f_{max}	$\sigma_{m\ (+)}$	$\sigma_{m\ (-)}$	γ	H_s (m)	θ_m (grid relative)
Spring (Significant)	10	TMA	10	9	6.89	0.165	0.20	15	17	1.0	1.66	30°
Summer (Significant)	10	TMA	9	9	6.01	0.180	0.225	10	19	7.0	1.25	30°
Fall (Significant)	10	TMA	9	9	6.51	0.180	0.225	25	25	7.0	1.83	38°
Winter (Significant)	10	TMA	9	9	6.52	0.170	0.225	20	27	3.0	1.69	30°
50-yr Storm	10	TMA	7	5	10.3	0.096	0.125	5	5	1.0	7.22	5°
γ = Directional Peak Enhancement Factor (adjusted to fit seasonal spectra) σ_m = Directional Spreading Parameter												

A storm surge value was also included in the wave modeling simulation to represent the increased water level experienced during the passage of a large storm event. Surge values for 25 storms from 1772 to 1969 (Chermock, et al., 1974) were used in an extremal analysis to estimate the value of a 50-year storm surge. A storm surge height of 3.0 m was determined from the extremal analysis and used as input for model simulations.

4.3 GRID GENERATION

4.3.1 Existing Conditions

In REF/DIF S, the reference grid consists of a mesh of points with dimensions IR and JR, as shown in Figure 4-14. At each point within the domain, water depth, as well as ambient current data, can be specified. Reference points are separated by spacing DXR (x-direction) and DYR (y-direction). Because REF/DIF S uses at least 5 points per wavelength of the shortest modeled wave, reference grid selection is not always trivial. In addition, boundaries of the model domain should be outside of the study area of interest, so that interference from the boundaries does not affect modeling results.

The model domain for the present study is divided into two reference grids due to the large region that is required for wave transformation numerical modeling. The western grid (Grid A) is used to focus on the Dauphin Island coastline, whereas the eastern grid (Grid B) is used to evaluate changes along the coastline of Morgan Peninsula. The two reference grids overlap near the entrance to Mobile Bay to include potential effects from tidal flow in both grids.

Grids A and B were created from the most recent bathymetric information available (see Section 3). The offshore grid boundary was selected to correspond closely to the location of WIS stations used to develop spectral input. Table 4-7 presents the UTM coordinates for the corners of each of the reference grids.

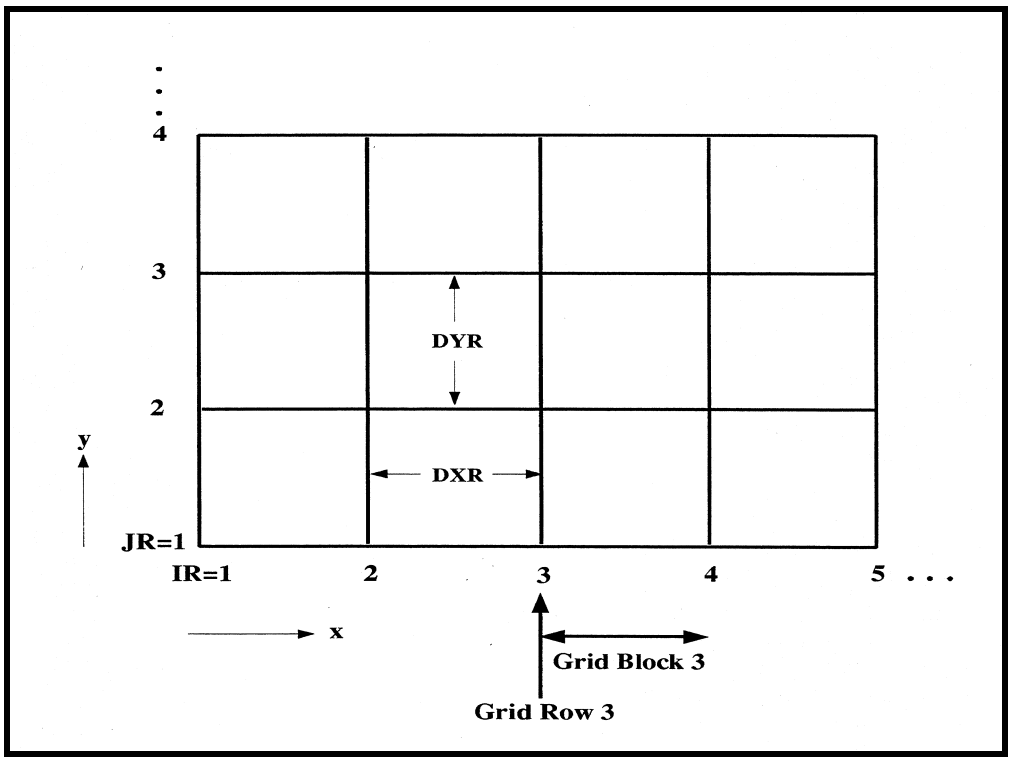

Figure 4-14. Illustration of reference grid notation (Kirby and Özkan, 1994).

Table 4-7. Reference grid dimensions.		
Reference Grid	UTM Easting extents (m)	UTM Northing extends (m)
A	363,797 to 409,597	3,317,290 to 3,350,690
B	392,900 to 442,700	3,317,290 to 3,350,690

The reference grids cell size is 200 by 200 m with interpolated depths obtained from the bathymetric data at each grid intersection point. The interpolated depths were smoothed using a 5-point matrix smoothing routine. Figure 4-15 (Grid A) and 4-16 (Grid B) show the associated bathymetric grids, sand resource areas, and subgrids for each study region, as well as the location of WIS and NOAA stations in the region.

Although the reference grid spacing was fixed at 200 m, subgrids and other input parameters allow REF/DIF S to calculate information at intermediate points within the reference grid. Depths at intermediate points are computed by REF/DIF S by fitting a twisted surface to the reference grid through linear interpolation. In the alongshore direction, the grid was subdivided by ten to yield a spacing of 20 m. This subdivision spacing was chosen to optimize computational time versus spatial resolution in the longshore direction, as well as to provide adequate information for nearshore sediment transport modeling. In the onshore direction, REF/DIF S automatically subdivides each reference grid step by the smallest calculated wavelength in the spectrum. Therefore, the onshore spacing varies throughout the domain as a function of the propagating wave field, unless the model is in a subgrid region. In areas where a subgrid is specified, the onshore subdivision must be fixed to correspond to the defined subgrid spacing (i.e., locations where depths and currents are specified).

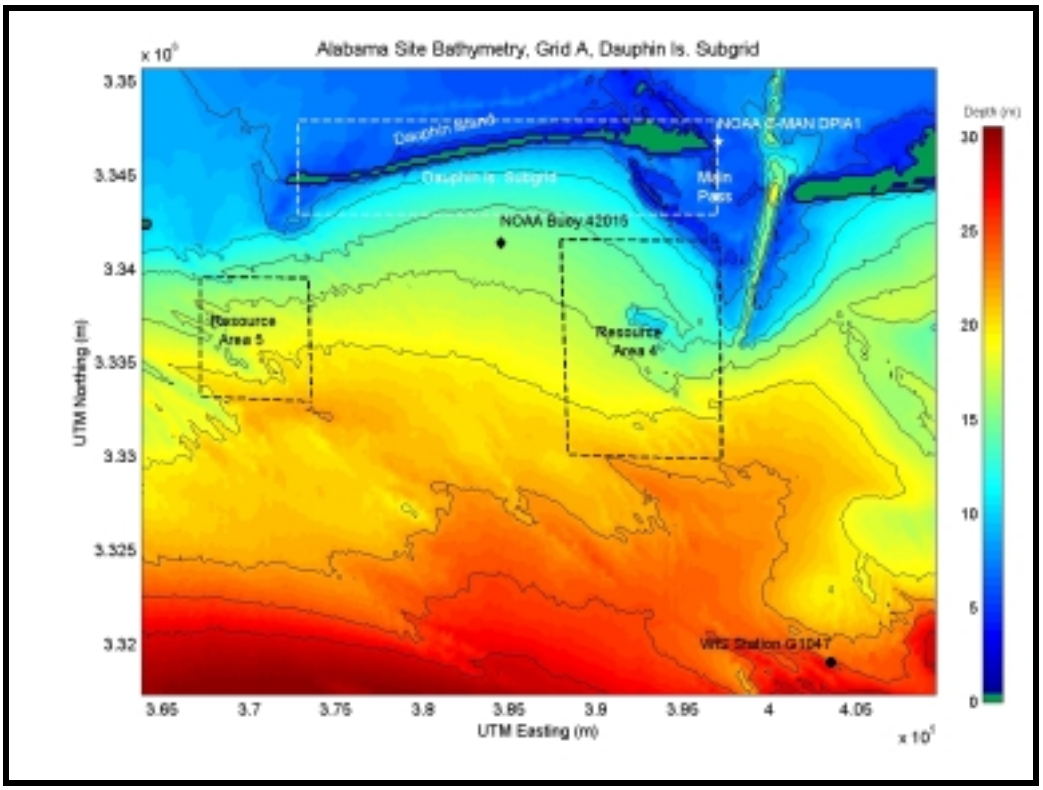

Figure 4-15. Bathymetry for Reference Grid A (Dauphin Island), with locations of WIS and NOAA stations, the defined sand resource areas, and the nearshore Dauphin Island subgrid.

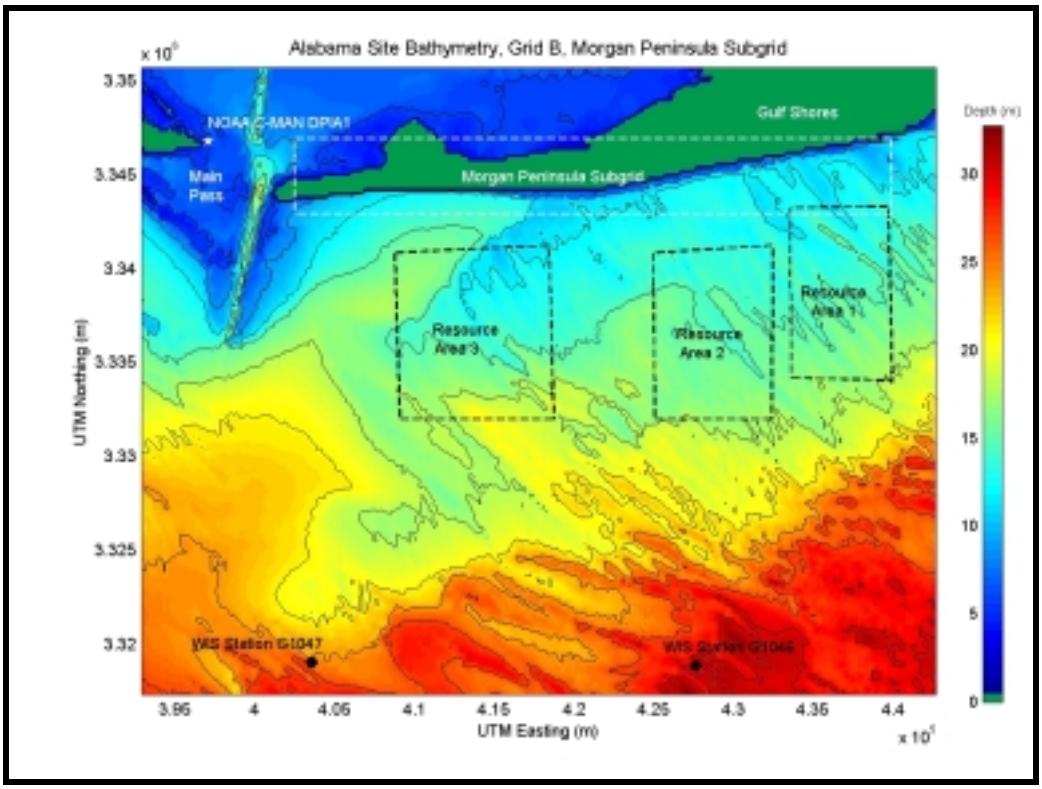

Figure 4-16. Bathymetry for Reference Grid B (Morgan Peninsula). With locations of WIS and NOAA stations, the defined sand resource areas, and the nearshore Morgan Peninsula subgrid.

Nearshore subgrids were created in the reference domains for Dauphin Island and Morgan Peninsula shorelines. Subgrids were used to generate detailed results in the nearshore zone as input to nearshore circulation and sediment transport models. Table 4-8 presents the dimensions and extents of each of the subgrids, as shown in Figures 4-15 and 4-16. Wave heights, water depth, and radiation stress results were output from each grid node in the subgrid domain.

Table 4-8. Subgrid dimensions.

Reference Grid	Subgrid	Onshore Spacing (m)	Alongshore Spacing (m)	UTM Easting extents (m)	UTM Northing extents (m)
A	Dauphin Is.	5	20	372,797 to 396,997	3,342,890 to 3,347,890
B	Morgan Peninsula	5	20	402,500 to 439,900	3,342,890 to 3,346,690

4.3.2 Post-Dredging Scenarios

4.3.2.1 Sand Borrow Site Selection

Four offshore borrow sites were identified as potential sources of beach quality sediment (see Section 7.0 for details); these data were used to numerically excavate wave modeling grids to simulate the impacts dredging may have on physical processes in the region (e.g., wave transformation and sediment transport). Three borrow sites are located east of Main Pass, one each within Sand Resource Areas 1, 2, and 3 (Figure 4-17). The final potential borrow site is located within Sand Resource Area 4 (Figure 4-18).

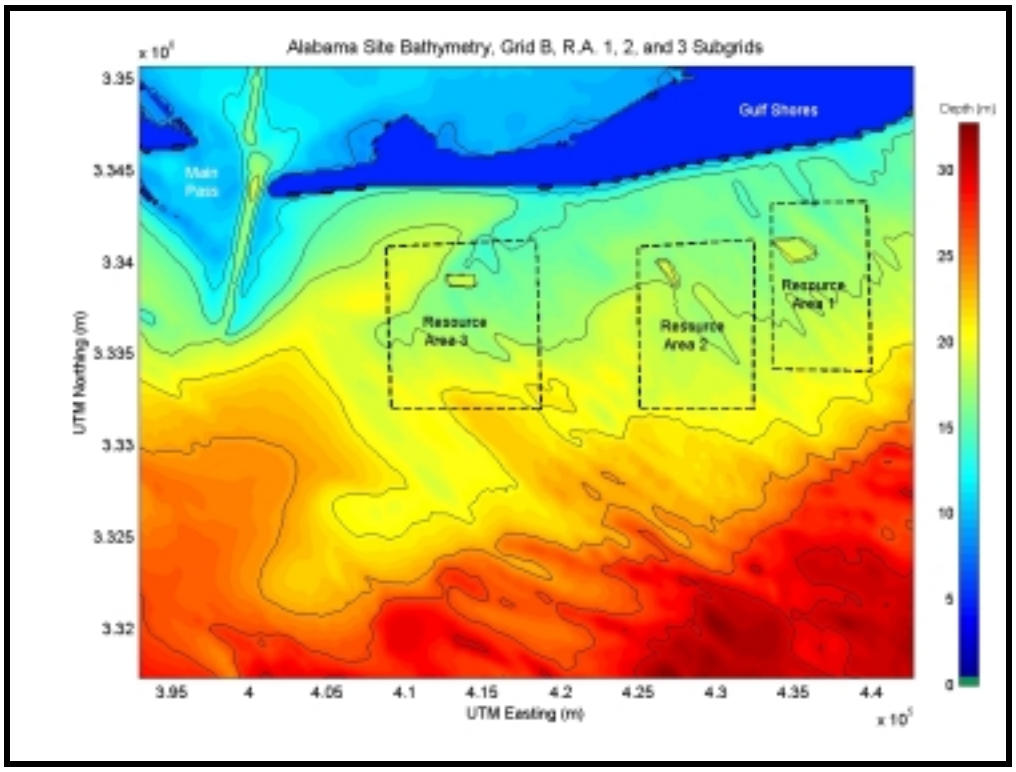

Figure 4-17. Potential borrow site locations (solid black lines) east of Main Pass.

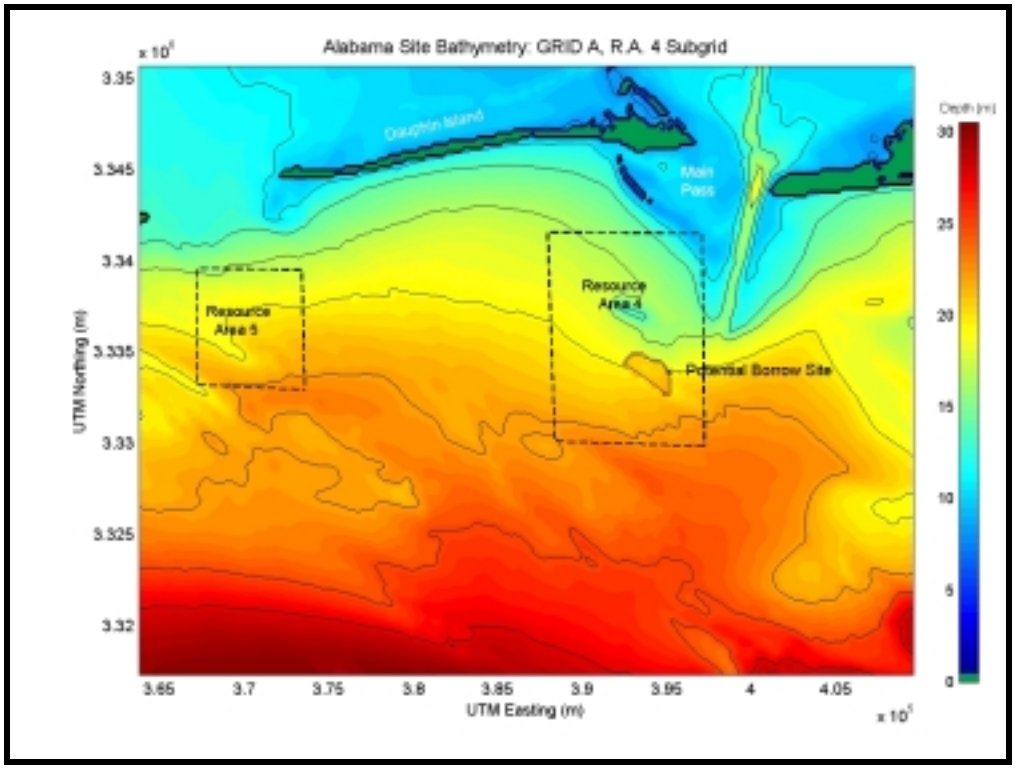

Figure 4-18. Potential borrow site location (solid black line) in Sand Resource Area 4.

The areas and volumes of the potential sand borrow sites were selected using the following guidelines.

- Sand Resource Areas - borrow site selection was limited to regions within the sand resource areas defined by the Mineral Management Service (MMS) and the Geological Survey of Alabama (GSA).
- Shoaling Regions - based on geomorphology within each sand resource area, regions characterized by shoaling features were selected. In this manner, the proposed dredging creates a flat bottom rather than a hole in the bathymetry surface. In addition, shoaling indicates regions that should replenish more quickly than others.
- Thickness of Sediment Layer - depth of dredging was based on the thickness of available sediment at each borrow location. The thickness of the sediment layer was determined from GSA core data sets.
- Extreme Dredge Scenarios - dredge volumes were selected to represent large sediment extraction scenarios or cumulative impact scenarios (e.g., dredging the same region before it replenishes with sediment). Although it is unlikely that the total sand volume extracted in the scenarios would ever be reached, extreme dredge scenarios are useful for evaluating at potential long-range and extreme impacts caused by sand dredging. The large borrow sites will have a greater impact on the physical processes, and therefore, indicate worst case situations.
- Beach Quality Sediment and Proximity to Nourishment Locations - the selection of borrow sites also considered the quality of beach compatible sediment and the relative proximity to nourishment locations.

Each of the four borrow sites were numerically dredged to simulate post-extraction scenarios. In the eastern reference modeling grid (Grid B), borrow sites within Sand Resource Areas 1, 2, and 3 are dredged simultaneously to simulate the combined impact from all three borrow sites and limit the number of model simulations.

4.3.2.2 Numerical Excavation of Gridded Surfaces

Following the selection of potential dredging locations, four sand resource areas were numerically excavated to evaluate the impact of bathymetry changes on wave transformation, nearshore circulation, and the beach and borrow location sediment transport. The depths of the sand borrow areas were increased to reflect the effects of potential dredging scenarios. Table 4-9 lists the sand resource areas where each numerical excavation was performed, as well as the excavation depth and resulting dredged sand volume. For example, if the pre-dredging depth at a grid point within Sand Resource Area 1 is 16 m, the post-dredging depth is increased to 19 m. As the wave field propagates into the grid, it is affected by a number of factors, including the increased water depth at the dredged location.

Table 4-9. Dredged depth and resulting sand volume within respective sand resource area.

Sand Resource Area	Depth to be Dredged (m)	Resulting Sand Volume(x 10^6 m^3)
1	3	5.8
2	3	1.7
3	4	4.7
4	3	8.4

Figure 4-19 illustrates the size, shape, and location of each borrow site within the sand resource areas. Because each grid consists of hundreds of cells, every grid point in the model domain has a water depth associated with it. Therefore, each grid point within the dredged borrow site can be artificially deepened to simulate effects of various dredging scenarios.

4.4 PRE-DREDGING RESULTS

4.4.1 Seasonal Simulations

Model simulations were performed for existing conditions (pre-dredging) with seasonal spectra and a 50-yr storm spectrum. This section discusses results for simulations of existing conditions. Figure 4-20 illustrates REF/DIF S results for the Dauphin Island grid (Grid A) for a typical spring season. The color map corresponds to the distribution of significant wave height (m) throughout the modeling domain. Solid black lines represent bathymetric contours. Land masses are shown in brown and are represented as thin film layers in REF/DIF S. Therefore, some wave energy is able to advance beyond the narrower sections of coastline into Mobile Bay and Mississippi Sound (e.g., the western end of Dauphin Island). Similar plots for a typical spring season can be found in Appendix B2.

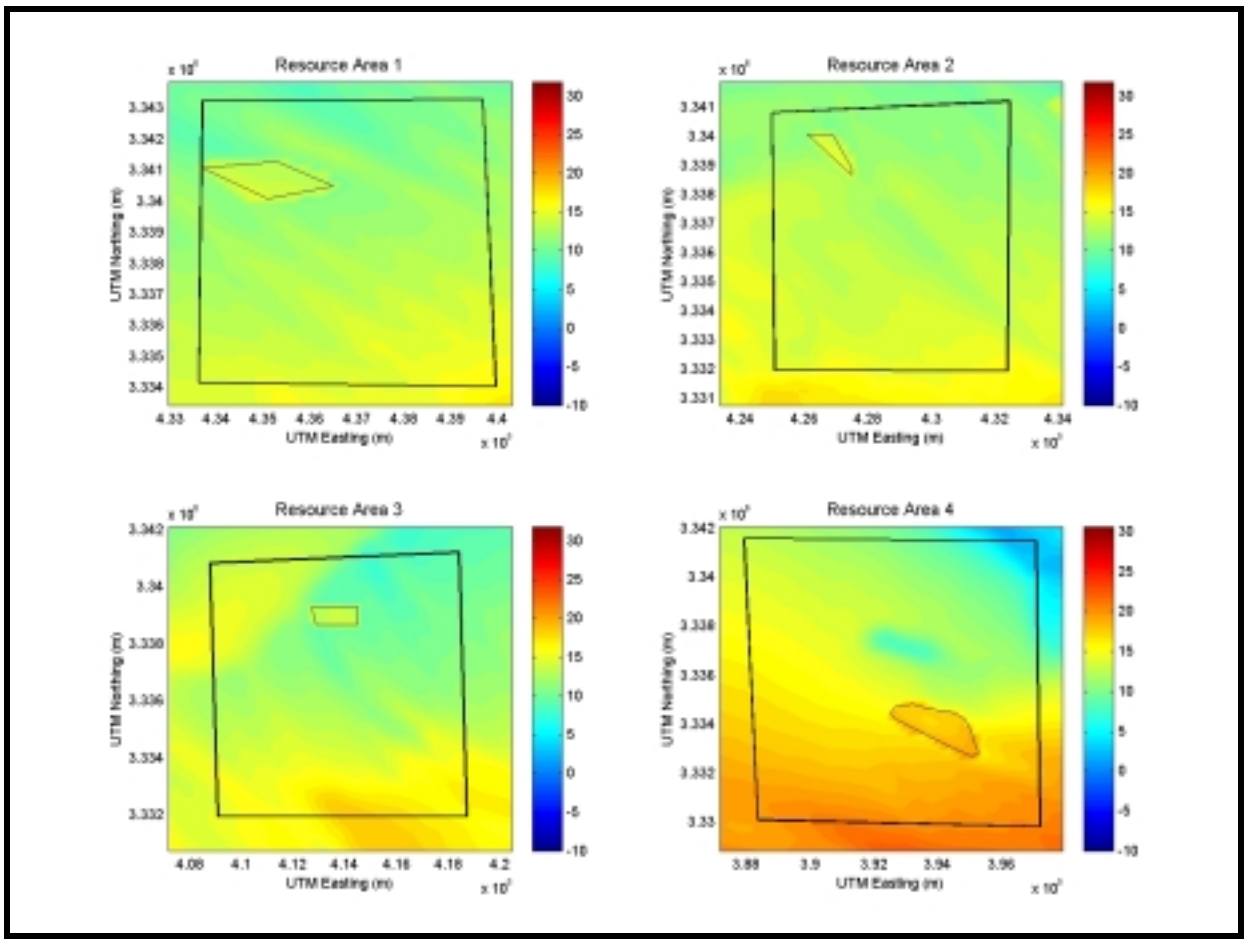

Figure 4-19. The four sand resource areas (outlined by the thick black line) and associated borrow sites (indicated by the thin black line).

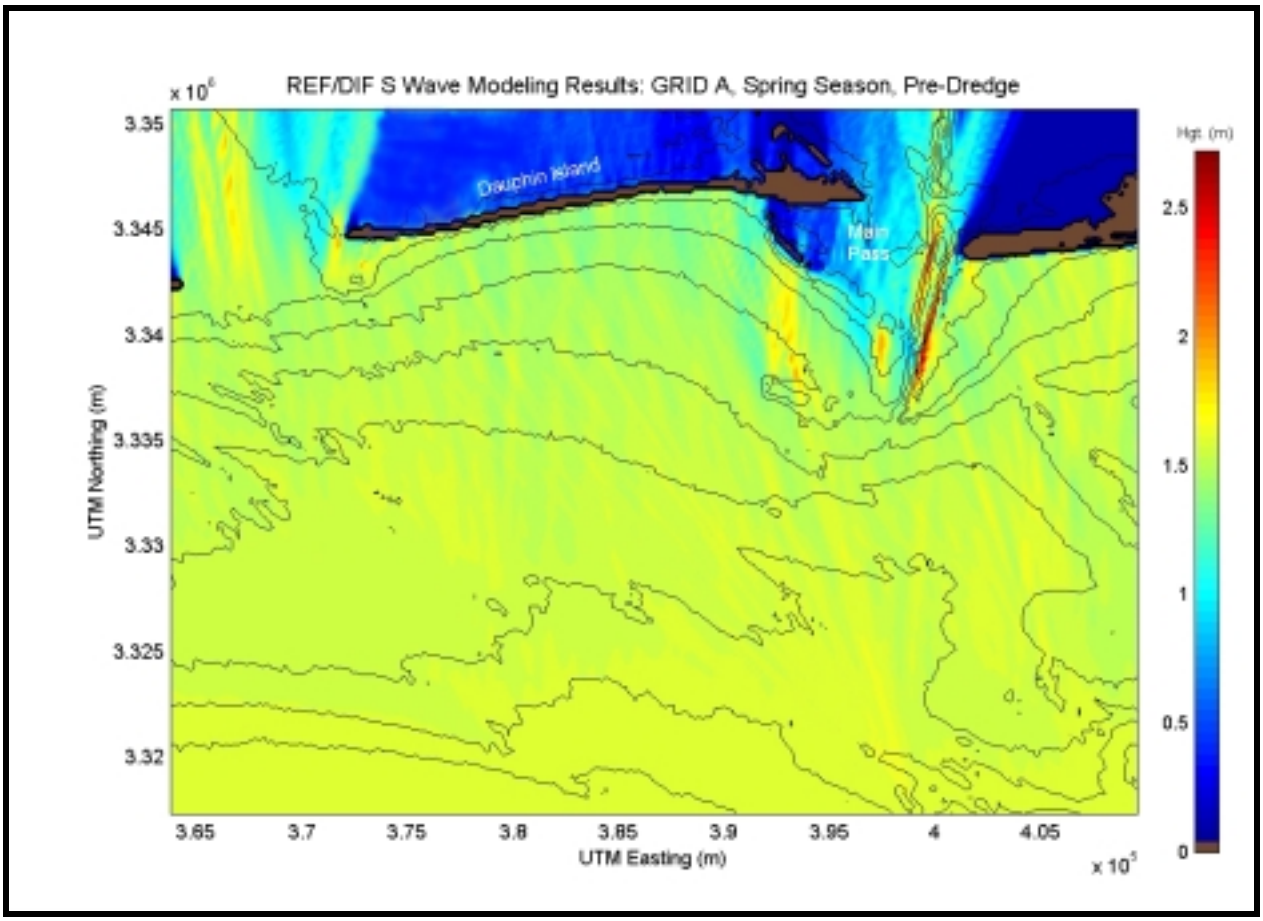

Figure 4-20. Spectral wave modeling results for existing conditions utilizing a typical spring season at reference Grid A.

There is minimal variation in wave heights in the offshore region for the spring simulation results (Figure 4-20). Because most of the spectral wave components do not interact with the seafloor at this depth, the wave field is not significantly affected by changes in bathymetry. The influence of bathymetry becomes significant at approximately the 15-m depth contour, where wave height and direction begins to change.

Wave focusing, divergence, and shadowing occur at several locations around Dauphin Island. Significant wave focusing is evident behind the Mobile Outer Mound disposal area. Wave refraction around this feature creates increased wave heights of approximately 0.25 to 0.5 m in the lee of the disposal area, and decreased wave heights adjacent to the mound. Wave focusing caused by Mobile Outer Mound produces an increase of energy that advances towards Pelican Island. Pelican Island offers a natural protective buffer against wave action for the eastern end of Dauphin Island, as indicated by the shadow zone behind the Pelican Island region. Wave focusing caused by Mobile Outer Mound most likely results in increased erosion at Pelican Island, which may significantly consume this protective wave buffer during a storm event.

An increase in wave height is also apparent west of the dredged navigational channel into Mobile Bay (397,500 Easting; 3,340,000 Northing). Bathymetric contours in this area focus wave energy into a region just before the eastern edge of the ebb shoal. The shape of contours in this

region causes waves to refract and converge. The resultant increase in wave height (approximately 0.5 m) dissipates quickly as the wave field propagates over the ebb shoal.

A similar increase in wave energy also is evident near the western end of Dauphin Island as the bathymetric contours refract the waves towards the western tip of Dauphin Island. Because the western end of Dauphin Island is the terminal end to net longshore sediment transport (east to west), an increase in wave energy in this region will not create significant erosion, though sediment transported into the region may be moved north and into Mississippi Sound as it encounters Petit Bois Pass. A significant amount of wave energy propagates through the pass between Dauphin Island and Petit Bois Island into Mississippi Sound as the bathymetry in this region remains relatively deep.

Another area of increased wave energy is located in regions adjacent to the dredged navigational channel (Main Pass) of Mobile Bay. Waves entering the region shoal in shallower areas (less than 5 m) adjacent to the dredged channel. Waves approaching from the southeast, as in the typical spring scenario, reform in deeper water of the navigation channel and shoal against the western edge of the channel.

Wave heights are relatively constant along the Dauphin Island shoreline. The eastern end of Dauphin Island is protected from significant wave energy by a shadow zone produced from Pelican Island and subaerial portions of the ebb shoals. A small amount of wave energy advances through the relatively narrow gap between the aerial and subaerial portions of the ebb shoal (approximately 394,000 Easting; 3,344,000 Northing).

The existing conditions simulation for the winter season, as presented in Appendix B2, produces results that are very similar to the results discussed for a typical spring season. Minor differences appear due to the increased significant wave height and subtle changes in the frequency and directional spread of the incident spectrum. Slightly larger wave energy increases are located in areas where wave shoaling was identified for the spring season, although the maximum increase is greater for the spring season near the dredged navigational channel into Mobile Bay.

During a typical summer season (figure presented in Appendix B2), average wave heights are significantly reduced (approximately 0.3 to 0.5 m) in regions where wave shoaling is apparent. Wave focusing caused by Mobile Outer Mound and regions near the dredged navigational channel is less concentrated and less severe. This is the result of a combination of reduced wave energy during the summer season, the change in peak spectral wave direction, and a broader directional spectrum. A slight increase in wave energy is allowed to proceed through the area between Pelican Island and the subaerial portion of the ebb shoal due to the angle of wave approach.

Fall season results (illustrated in Appendix B2) are similar to results for a typical summer season. Patterns of wave convergence and divergence during the two seasons are similar, with wave heights during the fall season 0.5 to 0.6 m higher than in summer.

Figure 4-21 illustrates results for a typical spring season along the Morgan Peninsula (Grid B). The color map corresponds to the distribution of significant wave height (m) throughout the model domain, while the solid black lines represent bathymetric contours. Similar plots for the entire season can be found in Appendix B2. As with Grid A, there is little variation in wave heights in the offshore region.

Areas of wave convergence and divergence seaward of the Morgan Peninsula shoreline are caused by the irregular bathymetry and the southwest-oriented seaward extending shoal located at approximately 414,000 Easting; 3,337,500 Northing. Wave energy converges in regions where bathymetric contours are aligned shore perpendicular as waves refract to match the bathymetry. In areas where bathymetric contours experience sudden changes in the along shore direction, wave convergence and divergence are apparent. Grid A simulations document an increase in wave height near the edges of the dredged navigational channel.

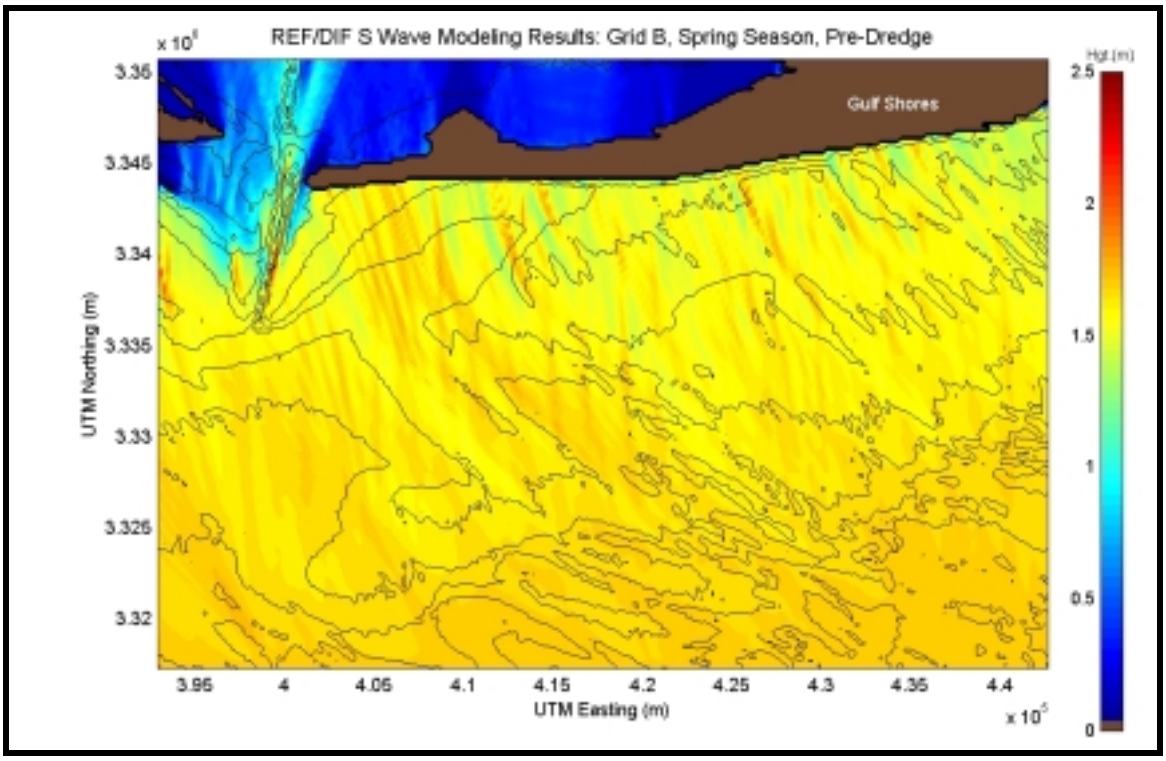

Figure 4-21. Spectral wave modeling results for existing conditions utilizing a typical spring season at reference Grid B.

Because of the irregular nature of the nearshore shoals, wave approach angles experience significant changes on the continental shelf. Summer, fall, and winter season results for Morgan Peninsula (presented in Appendix B2) indicate similar patterns of wave convergence and divergence. There are no visible differences in wave height patterns for different seasons. The winter season is slightly more energetic (wave heights approximately 0.2 to 0.3 m greater). Spring and fall results are almost identical, with only a slight variation in directional spreading.

4.4.2 High Energy Wave Events Results

Figure 4-22 illustrates wave transformation results for the 50-yr storm at Dauphin Island (Grid A). Fifty-year storm results for Morgan Peninsula are presented in Appendix B2. Storm wave propagation patterns are similar to those documented for seasonal trends. For example, Mobile Outer Mound now concentrates a 4.0- to 4.5-m wave field on southeastern Pelican Island and a significant reduction in wave height is evident adjacent to this area. Wave shoaling in other areas (e.g., the dredged navigation channel) appears to be less important when considering larger storm waves, though the increased color scale (Figure 4-22) reduces visible identification of previously significant wave height modifications (shown in Figure 4-20). Wave approach directions are modified further offshore since the large storm waves interact with the seafloor in deeper water than average seasonal waves.

Due to the reduced number of spectral components used with storm simulations (closer to a monochromatic simulation) and the increased wave height, increased patterns of convergence and divergence are more evident in model results. These streaks are typically caused by large variations in bathymetry in the modeling grid. Comparison of pre- and post-dredging results in the next section will not include existing areas of convergence and divergence, but will concentrate only on changes caused by the dredging scenarios.

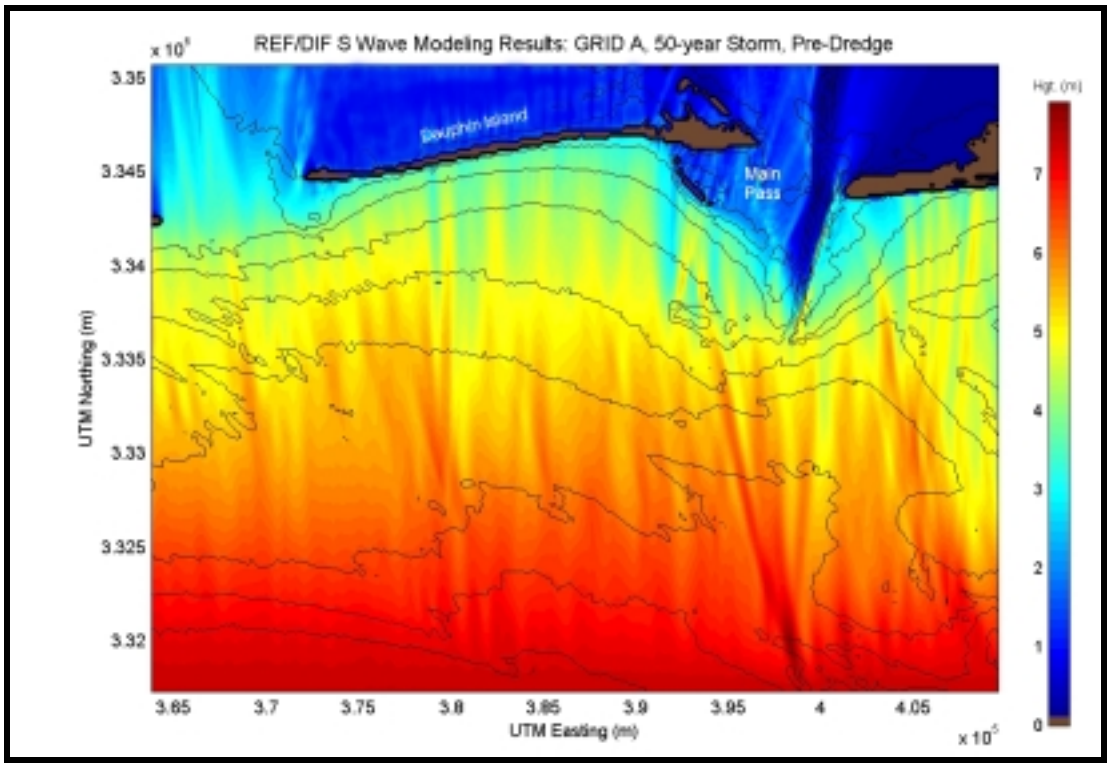

Figure 4-22. Spectral wave modeling results for existing conditions simulating a 50-yr storm event at reference Grid A.

4.4.3 Model Results Relative to Historical Shoreline Change

When comparing average seasonal wave modeling results to historical shoreline change, the overall influence of each season on coastal and nearshore change can be investigated. Figure 4-23 shows significant wave heights extracted along a baseline 100 m seaward of the Dauphin Island coastline. The seasonal results, an average result for all four seasons, and the 50-yr storm result are illustrated on the panels within the figure. Historical shoreline change for Dauphin Island is represented by a thick line and is scaled by the left-hand axis. Significant wave height is represented by a thin line and is scaled by the right-hand axis.

Historically, the western portion of Dauphin Island has been dominated by lateral island growth and shoreline retreat. The eastern end illustrates accretion in the shadow zone behind Pelican Island and relative stability near Mobile Bay entrance since 1847. A small erosional area is located landward of the gap between Pelican Island and subaerial portions of the ebb shoal, where wave energy propagates landward, as indicated in the wave model results presented above. Wave height distribution correlates with shoreline change rates relatively well. Wave heights are generally higher in areas that have experienced historical shoreline retreat, while wave height reduction is indicated in areas of historical accretion (e.g., the shadow zone behind Pelican Island). Wave heights during the summer season are smaller than in other seasons. Therefore, it is expected that less erosion or accretion occurs during that portion of the year. The 50-yr storm exhibits higher wave heights along the entire coastline, yet still maintains a form similar to the seasonal results. The correlation between wave height results and historical shoreline change rates suggests that the wave model is performing reasonably.

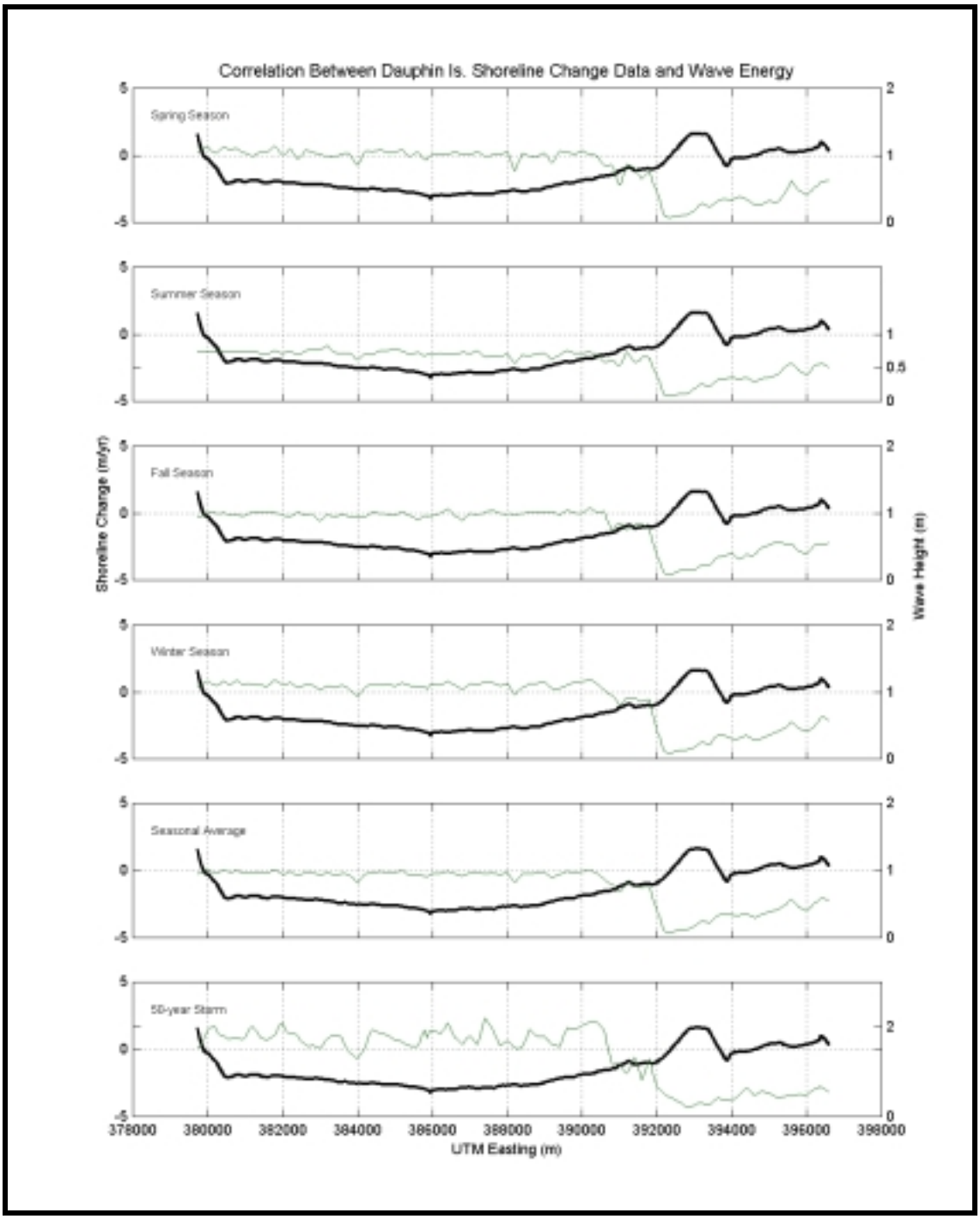

Figure 4-23. Wave height (thin line) taken from a baseline 100 m seaward of the Dauphin Island shoreline compared with historical shoreline change rates (thick line; 1847/67 to 1978/82). Points along the coastline that indicate increased wave height correspond to areas of historical erosion, while areas of historical accretion correspond to reduced wave heights.

Figure 4-24 shows similar results for the Morgan Peninsula. Historical shoreline change rates indicate a relatively stable coastline with accretion occurring at the western end of the peninsula (again due to the dominant sediment transport to the west). Significant wave heights presented in Figure 4-24 were smoothed using a weighted 11-point filter to identify general trends in wave height. Correlation between wave heights and historical shoreline change rates can again be made at certain points along the coast. For example, a region of historical erosion evident at approximately 432,500 m (Easting), is also indicated as an area of increased wave energy. In addition, wave heights increase from west to east along Morgan Peninsula. Smaller wave heights exhibited at the western end of the peninsula may also contribute to the accretion trend seen in shoreline change rates.

In a regional context, shoreline change and wave height distribution correlate well along Morgan Peninsula. However, slight changes in the orientation and location of offshore shoals result in a shift in the location of areas of energy convergence and divergence. Historically, these shore-oblique shoals have experienced some movement, thereby changing the location of increased wave energy along the coast.

4.5 COMPARISON OF PRE- AND POST-DREDGING RESULTS

4.5.1 Post-Dredging Results

Following wave modeling runs for existing conditions, simulations were performed for post-dredging scenarios. Results were produced for each of the seasonal spectra and the 50-yr storm event to evaluate potential physical impacts of offshore sand mining. Figure 4-25 presents the results for Dauphin Island (Grid A) simulating a typical spring season for the post-dredging scenario in Sand Resource Area 4. As in Figure 4-20, the color map corresponds to the distribution of significant wave height (m) throughout the model domain. The solid black lines represent bathymetric contours. Other than the differences in bathymetry, the same boundary conditions were used in the simulation to produced results shown in Figure 4-20.

The same wave patterns described in Section 4.4 are evident in the post-dredged model results (e.g., the wave focusing behind Mobile Outer Mound; the increase in wave height along the edges of the dredged navigational channel). It is difficult to visually identify any significant differences between the pre- and post-dredging results. This is true for all seasonal and 50-yr storm simulations. Because the modifications to the wave field are not very evident after initial inspection of results, the impact of the potential sand mining operations on the wave field can be considered small compared with natural changes occurring throughout the model domain. Figures similar to Figure 4-25 for all the simulated post-dredging model results can be found in Appendix B3.

4.5.2 Existing Conditions Versus Post-Dredging Seasonal Results

Differences in wave heights (between pre- and post-dredging results) were computed at each grid point within the model domain to document potential impacts caused by specific sand mining scenarios. Pre-dredging wave simulations were subtracted from the post-dredging wave results so that positive (negative) differences indicate an increase (decrease) in wave height related to sand mining at potential borrow sites. Figure 4-26 shows the difference plot for the spring season presented above. As expected, sand mining creates a zone of decreased wave energy behind the sand borrow site and increased energy adjacent to the borrow site. A maximum increase of approximately 0.17 m (11% increase relative to offshore significant wave height) and a maximum decrease of 0.2 m result from the sediment extraction scenario for Resource Area 4 (Table 4-9) during the typical spring season. Increased wave energy is focused near the southwest end of Pelican Island and on the eastern end of Dauphin Island. Increased wave heights dissipate relatively quickly once breaking begins. A decrease in wave energy is evident in the lee of the borrow site, and therefore reduces the magnitude of wave height focused by the Mobile Outer

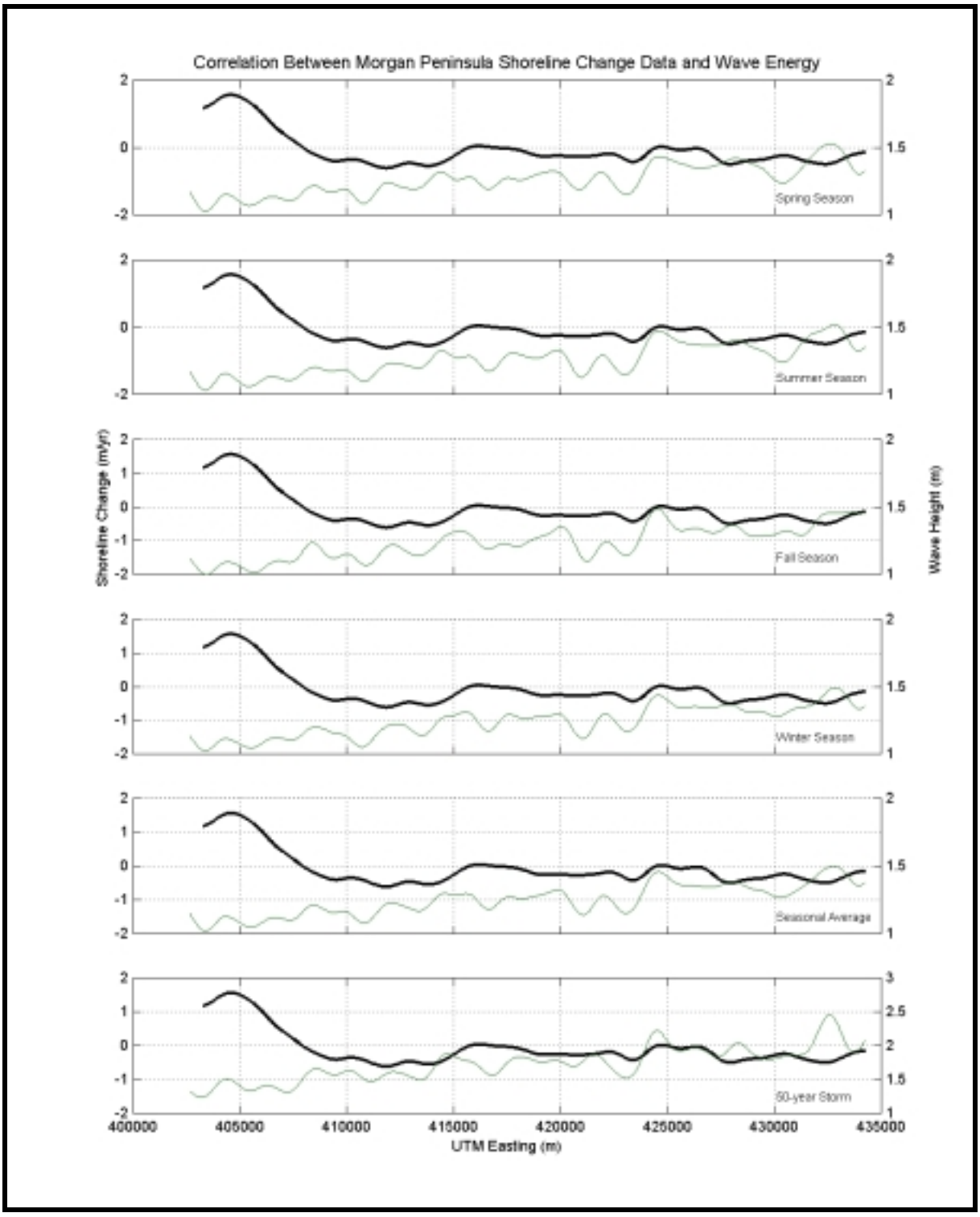

Figure 4-24. Wave height results (thin line) taken from a baseline 100 m seaward of the Morgan Peninsula shoreline compared to historical shoreline change rates (thick line; 1847/67 to 1978/82).

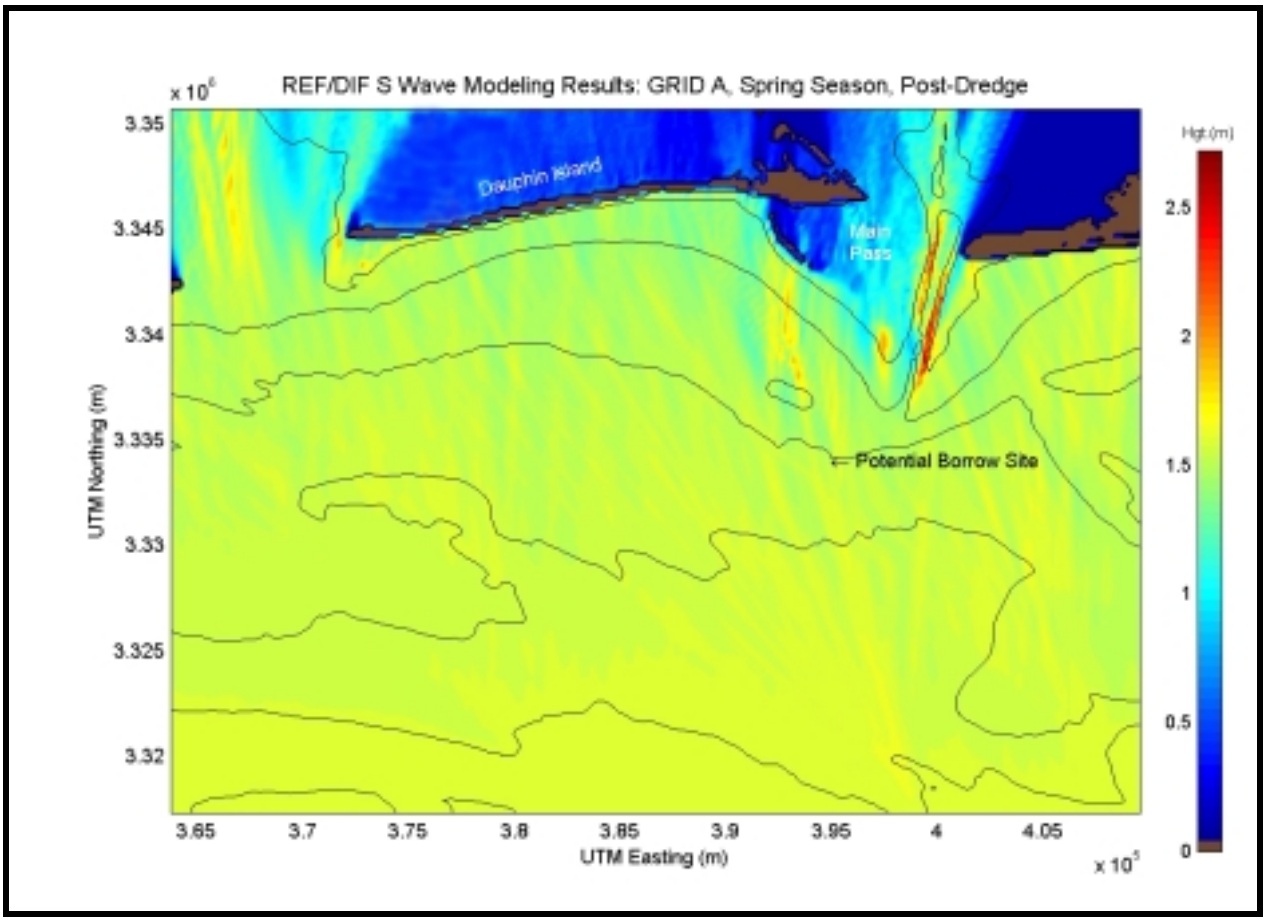

Figure 4-25. Spectral wave modeling results for post-dredging scenario utilizing a typical spring season at reference Grid A.

Mound. Because wave energy focused on Pelican Island is reduced during a typical spring season, potential sand mining operations may be beneficial for protecting Pelican Island.

Difference plots for the remaining simulations at Grid A are presented in Appendix B4. Winter season differences indicate a slight shift in the impact zone to the east due to variations in peak spectral wave approach. The magnitude of wave height differences is slightly smaller than the spring simulations and the western edge of Pelican Island experiences an insignificant increase in wave height (0.02 to 0.04 m).

For fall and summer seasons, wave transformation trends were similar, and the impact of potential sand excavation scenarios was insignificant (changes less than 0.06 m). During the summer season, waves were smaller, consisted of shorter periods, and the directional spread was quite wide. Modifications to the wave field were not well-defined, and changes were negligible. The fall season model runs produced slightly larger changes in wave height differences on a portion of Pelican Island; however, changes were determined to be insignificant (5- to 6-cm increase) relative to source wave data (WIS). Overall, modifications to the wave field are insignificant during the fall and summer.

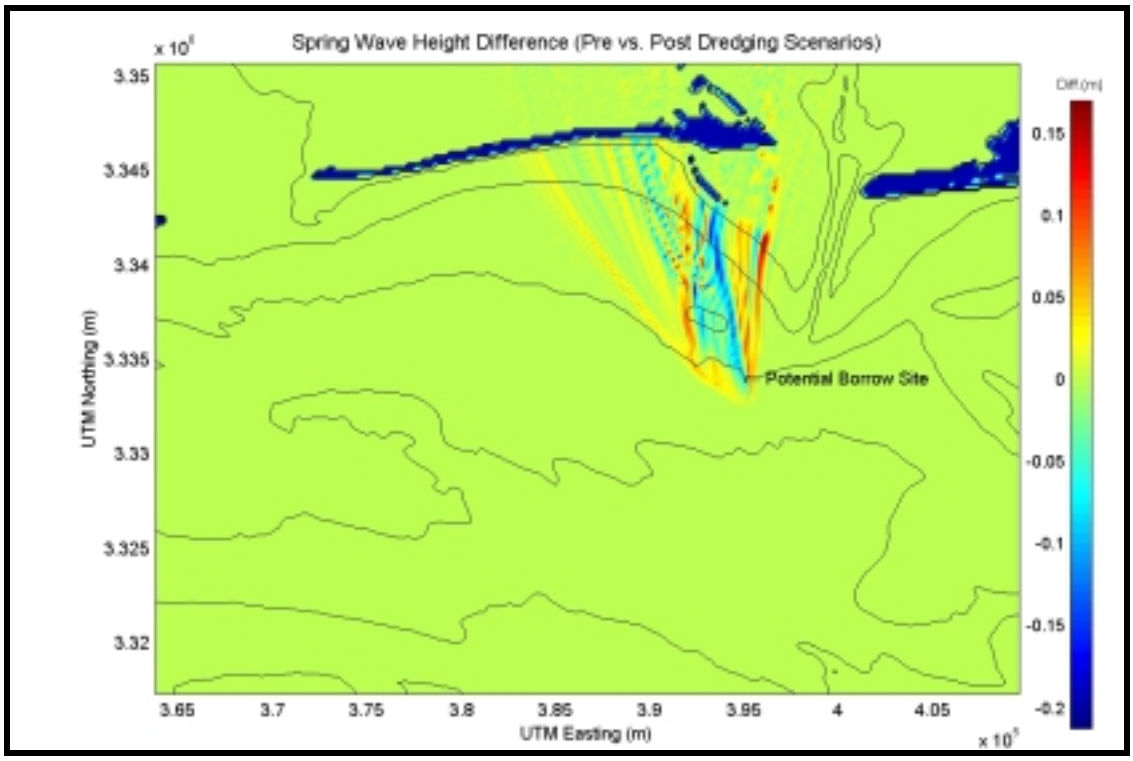

Figure 4-26. Wave height modifications resulting from potential offshore mining at Sand Resource Area 4 for a typical spring season. Hot colors (reds) identify areas of increased wave height, while cold colors (blues) identify areas of decreased wave height.

Figure 4-27 illustrates wave height differences for the spring season at Grid B (Morgan Peninsula). Wave heights were modified by the dredged regions as waves are refracted away from each borrow site by local changes in water depth, creating a shadow zone directly behind the borrow site and an increase in wave height in adjacent waters. This phenomena is evident at all three of the proposed sand borrow sites within Grid B. A maximum wave height increase of 0.4 m (24% increase) at the western edge of Sand Resource Areas 2 and 3 is caused by the large sediment extraction scenarios (Table 4-9) for the typical spring season. A maximum decrease of 0.4 m is evident in the lee of the dredged locations. The shadow zone behind the Sand Resource Area 2 borrow site is more concentrated due to the orientation of the dredged area. Wave height modifications are larger for borrow sites within Grid B, with maximum changes in significant wave height approaching 0.3 to 0.4 m. The increase in wave height is due to borrow-site location relative to the shoreline and borrow site size and orientation. However, waves dissipate energy as they advance toward the shoreline and negligible increases in wave height (0.1 m or less) are observed at potential impact areas along the coastline.

Difference plots for the remaining simulations at Grid B are presented in Appendix B4. During the summer, winter, and spring, patterns of wave modifications are comparable. Maximum increases/decreases in wave height are slightly smaller ($\pm$ 0.2 to 0.3 m) than observed during the spring season. In the fall, modifications to the wave field are less consolidated due to the less direct wave approach direction. During the summer and winter, a small area of increased wave height observed at the western edge of the borrow site within Sand Resource Area 3 appears to propagate to the shoreline (at approximately 412,500 Easting; 3,344,000 Northing). However, changes at the shoreline are negligible.

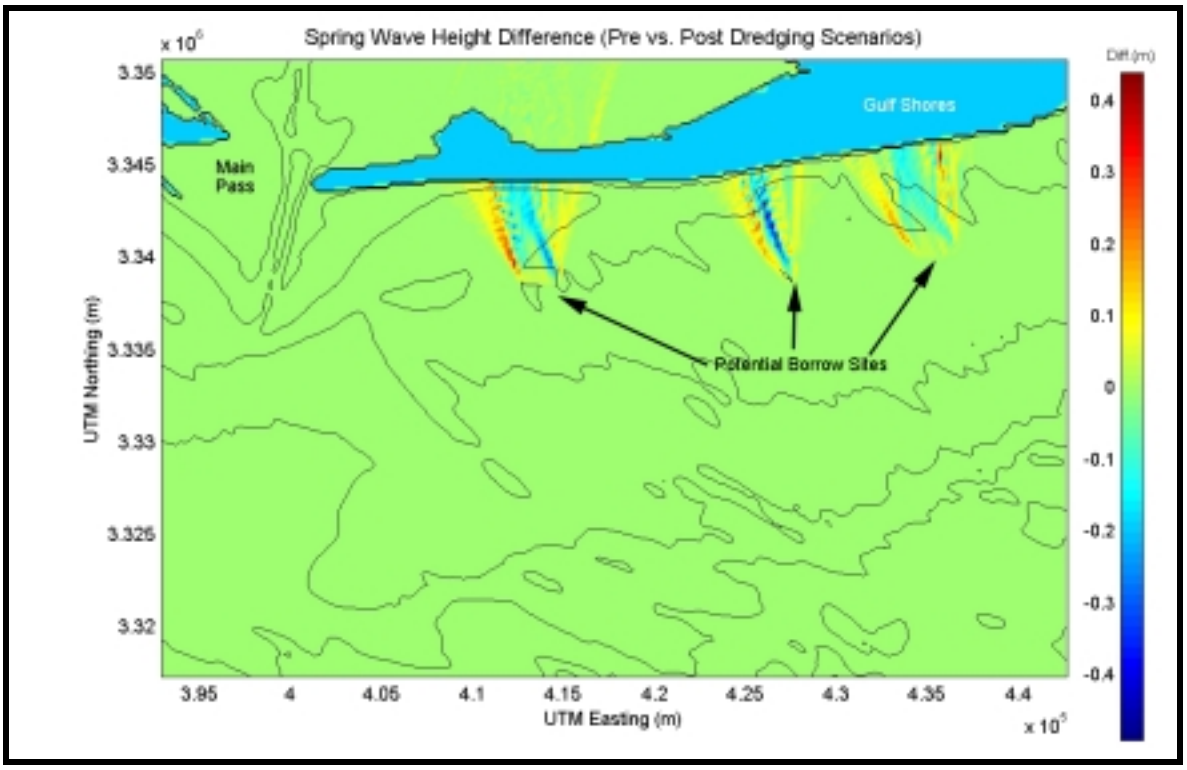

Figure 4-27. Wave height modifications resulting from potential offshore mining at Sand Resource Areas 1, 2, and 3 for a typical spring season. Hot colors (reds) identify areas of increased wave height, while cold colors (blues) identify areas of decreased wave height.

Overall, the impact caused by potential offshore dredging at sand borrow sites during normal conditions is relatively small. At most, only minor changes are expected in the wave field and the nearshore sediment transport potential.

4.5.3 High Energy Wave Event Results

Differences in wave heights were also computed for 50-yr storm simulations to identify potential impacts of offshore sand mining. Figures 4-28 and 4-29 show results for Dauphin Island and Morgan Peninsula, respectively. A similar distribution of wave energy change as that indicated in the seasonal results is illustrated (i.e., wave energy reduction directly behind the dredged area and an adjacent increase in energy). Both change plots indicate a maximum increase in wave height of approximately 1.5 m (20% increase over offshore wave heights). A wave reduction of 1.5 to 2.0 m is observed in the shadow zones of borrow sites.

In Grid A (Dauphin Island), a significant amount of wave energy is dissipated before the waves reach the shoreline as modifications to wave heights are less than 0.5 m along a majority of Pelican Island. As with seasonal results, an beneficial reduction in wave height is obtained due to borrow site characteristics and Mobile Outer Mound for a portion of Pelican Island. However, a smaller amount of the wave energy dissipates before reaching the shoreline landward of borrow sites in Sand Resource Areas 1, 2, and 3. Therefore, during storm events, changes may be large enough to result in significant impacts at certain locations along the eastern Alabama shoreline.

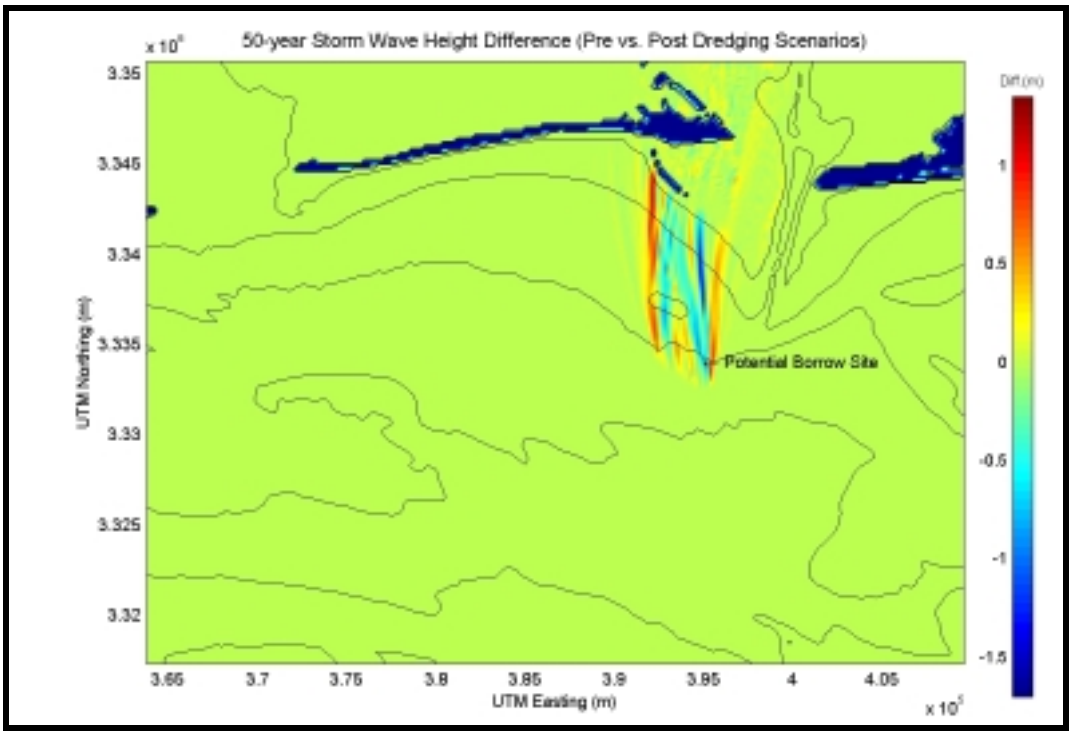

Figure 4-28. Wave height modifications resulting from potential offshore mining in Sand Resource Area 4 for a 50-yr storm event. Hot colors (reds) identify areas of increased wave height, while cold colors (blues) identify areas of decreased wave height.

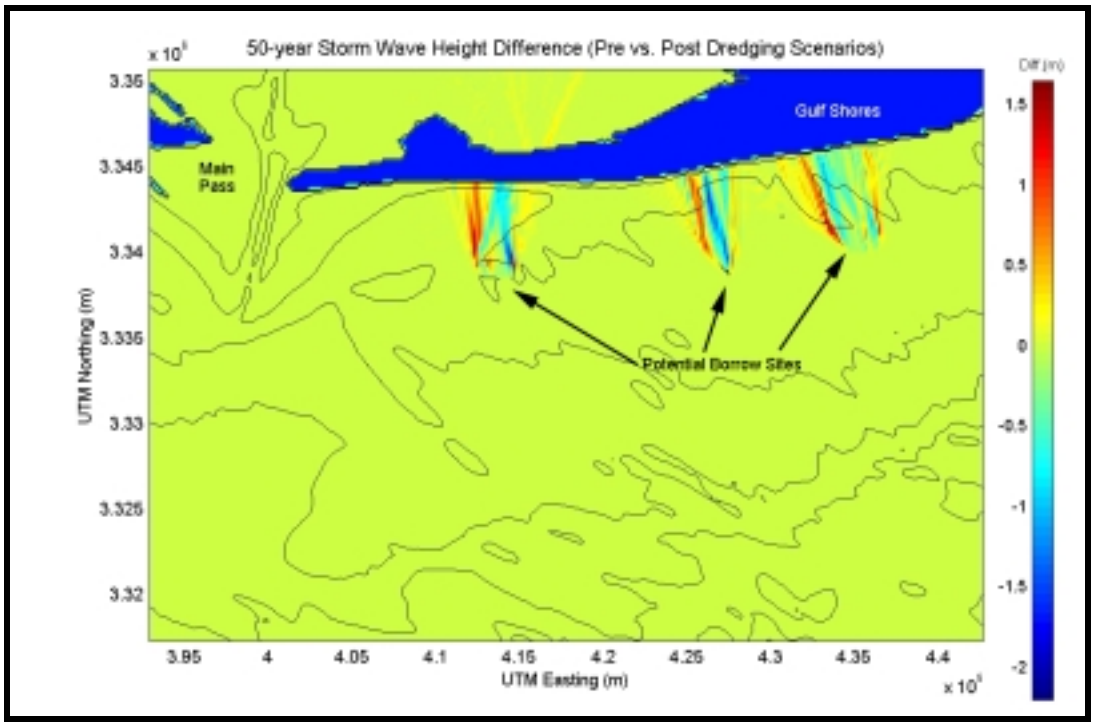

Figure 4-29. Wave height modifications resulting from potential offshore mining in Sand Resource Areas 1, 2, and 3 for the 50-yr storm event. Hot colors (reds) identify areas of increased wave height, while cold colors (blues) identify areas of decreased wave height.

4.6 DISCUSSION

This section presented an analysis of potential impacts to the nearshore wave climate caused by sand mining offshore Alabama. The analysis approach relied upon the spectral wave model REF/DIF S to simulate the behavior of a random sea state, incorporating the effects of shoaling, wave breaking, refraction, diffraction, and energy dissipation. Accuracy of the wave transformation model is affected by quality of the selected input data and parameters. Data analysis revealed a relatively consistent wave climate throughout the year (wave height, direction, periods, etc.). The Gulf of Mexico experiences minimal variation in wave climate, and with the exception of storm events, typical conditions are directionally narrow and energetically mild.

Wave transformation modeling simulations were performed for existing conditions with seasonal and 50-yr storm spectra. The model results identify key areas of wave convergence, divergence, and shadow zones offshore Alabama. In the seasonal simulations, significant wave heights experience little variation up to the 15-m depth contour where the wave field begins to feel the influence of bathymetry. For Dauphin Island, wave heights are relatively consistent along the shoreline while the eastern end of the island is protected from significant wave energy by Pelican Island and subaqueous portions of the ebb shoal. Several areas of wave convergence were identified in the Dauphin Island grid, including Mobile Outer Mound, which focuses wave energy on Pelican Island during most seasons. Wave focusing caused by Mobile Outer Mound results in an increase in erosion at Pelican Island, and during a storm event may significantly erode the island. Areas of wave convergence and divergence along the Morgan Peninsula are primarily caused by the southeast-oriented linear shoals on the continental shelf.

For the 50-yr storm, the wave patterns are similar to the normal seasonal results. An increase in wave height is significant in many areas where wave convergence occurs. For example, the Mobile Outer Mound disposal site concentrates 4.0- to 4.5-m wave heights on Pelican Island during an event of this kind. The 50-yr storm event simulated in the present study represents a major storm that will have significant impact on the approaching wave field and sediment transport patterns.

Differences in wave height between pre- and post-dredging scenarios offshore Dauphin Island indicate maximum wave height changes (increases and decreases) for seasonal simulations ranged from $\pm$ 0.02 to 0.2 m. These maximum changes dissipate relatively quickly as waves break and advance towards the coast. For the Morgan Peninsula, maximum wave height differences were larger ($\pm$ 0.2 to 0.4 m) due to borrow site sizes and orientations as well as proximity to the shoreline. However, the waves dissipate energy as they propagate towards the shoreline and increases in wave height of 0.1 m or less are observed at potential impact areas along the coast. Overall, the impact caused by the potential offshore dredging during normal seasonal conditions is negligible.

During extreme wave conditions (e.g., a 50-yr storm event), wave heights are modified up to $\pm$1.5 to 2.0 m, indicating a rather significant change. For the sand borrow site located in Sand Resource Area 4, a significant amount of wave energy is dissipated before the waves reach the coast. As such, wave height increases are less than 0.5 m along a majority of Pelican Island. During a storm event, waves are large (4 to 8 m), even without modifications caused by dredging. Therefore, a maximum change of 0.5 m (7% of the offshore wave height) may not significantly increase nearshore erosion above existing conditions near Dauphin Island.

Borrow sites within Sand Resource Areas 1, 2, and 3, which are located closer to the coast, have a greater impact on the wave field. A small amount of wave energy is dissipated before reaching the shoreline. Changes to the wave heights are large enough to result in significant impacts at certain locations along Morgan Peninsula. A moderate to large storm event will produce changes in the wave field and in the sediment transport patterns along the coastline.